FLUORESCENCE LIFETIME IMAGING MICROSCOPY (FLIM) SYSTEM FOR IMAGING OF ORAL CANCER AND PRECANCER

A Dissertation

by

SHUNA CHENG

Submitted to the Office of Graduate and Professional Studies of
Texas A&M University
in partial fulfillment of the requirements for the degree of

DOCTOR OF PHILOSOPHY

Chair of Committee,	Javier A. Jo
Co-Chair of Commettee,	Kristen C. Maitland
Committee Members,	Brian E. Applegate
	Jim Ji
Head of Department,	Gerard L. Cot é

December 2014

Major Subject: Biomedical Engineering

ABSTRACT

Standard diagnosis of oral cancer is based on visual inspection and palpation by a clinician followed by histological examination of one or more tissue biopsies. Choosing the right location for biopsies, which represents the most severe lesion, is difficult and subjective to each clinician's experience, especially for precancer lesions which are often diffuse, multifocal, and clinically indistinguishable from benign lesions. This may lead to low diagnosis sensitivity. The aim of this dissertation is to design a more sensitive and objective screening tool to guide the biopsy of oral cancer and precancer.

Fluorescence lifetime imaging microscopy (FLIM) is a noninvasive optical technique which is able to detect the information of tissue metabolism and biochemistry based on fluorescence as a source of contrast. Recently, there is increasing interest in the application of multispectral FLIM for medical diagnosis. Central to the clinical translation of FLIM technology is the development of compact and high-speed clinically compatible systems. In this dissertation, four multispectral FLIM systems were designed and built. A bench-top multispectral FLIM system was first built and combined with reflectance confocal microscopy (RCM) for the preclinical validation by imaging a hamster cheek pouch model of oral carcinogenesis. After that, in order to facilitate *in vivo* imaging of human oral mucosa, three different multispectral FLIM endoscopes were designed. The first FLIM endoscope was built based on a fiber bundle and the time-gated implementation by an intensified charged-coupled device (ICCD). The system was validated by imaging a hamster cheek pouch model of oral carcinogenesis. To achieve faster imaging speed and

more accurate lifetime estimation, two rigid handheld FLIM endoscopes were built based on a pulse sampling implementation. These two handheld endoscopes were different in weight and size. The more compact one might serve as the clinical prototype for oral cancer and precancer detection. Both systems were validated by imaging the human oral biopsy *ex vivo* and human oral mucosa *in vivo*. The development of these systems will facilitate the evaluation of multispectral FLIM for oral cancer and precancer detection.

DEDICATION

To my parents and my husband

ACKNOWLEDGEMENTS

I want to first thank my advisor Dr. Javier Jo, who has given me the chance to study and work in such a good research atmosphere. He has supported, guided, encouraged and spent countless time helping me through my five years as a graduate student.

I am grateful for Dr. Kristen Maitland, my co-advisor. Without her generous instruction, I could not have finished this study.

I want to thank Dr. Brian Applegate, who has given me many ideas and suggestions on system design.

I want to thank Dr. Jim Ji, who has sacrificed time and energy to serve on my committee.

I want to thank Dr. Lisa Cheng, Dr. John Wright and Lee Jordan at Baylor College of Dentistry for the help on imaging human oral cancer and precancer *ex vivo* and *in vivo*.

Last but not least, I want to thank all my colleagues who have always given me a lot of ideas and help on my research: Joey Jabbour, Rodrigo Cuenca, Bilal Malik, Jesus Rico, Paritosh Pande, Michael Serafino, Sebina Shrestha and Carl Johnson.

This work is supported by NIH R01CA138653, R01HL11136 and R21CA132433.

NOMENCLATURE

NCI	National Cancer Institute
FLIM	Fluorescence Lifetime Imaging Microscopy
RCM	Reflectance Confocal Microscopy
FOV	Field of View
UV	Ultra Violet
VIS	Visible
GRIN	Gradient Index
ICCD	Intensified Charged-Coupled Device
SNR	Signal to Noise Ratio
USAF	United States Air Force
MEMS	Micro-Electromechanical Systems
MCP-PMT	Micro-channel Plate Photomultiplier Tube
BS	Beam Splitter
DS	Dichroic Mirror
BF	Bandpass Filter
NADH	Nicotinamide Adenine Dinucleotide
FAD	Flavin Adenine Dinucleotide
IRB	Institutional Review Board
IACUC	Institutional Animal Care and Use Committee
TAMU	Texas A&M University

PBS	Phosphate Bufered Saline
H&E	Hematoxylin and Eosin
DMBA	7,12-dimethylbenz1/2α_anthracene
FWHM	Full Width Half Max
IRF	Impulse Response Function
RLD	Rapid Lifetime Determination
DMBA	7,12-dimethylbenz [α] anthracene
POPOP	1,4-bis (5-phenyloxazol-2-yl) benzene
FRET	forster resonance energy transfer
LSF	line-spread
PSF	lateral point spread function
GOI	gated optical intensifier

TABLE OF CONTENTS

Page

LIST OF FIGURES

Page

LIST OF TABLES

Page

1. INTRODUCTION

1.1 Motivation

Oral Cancer is defined as cancer that forms in the oral cavity or the oropharynx. The National Cancer Institute (NCI) estimates that around 42,440 new cases of oral cancer will be found in the United States in 2014 [1]. Although the incidence of oral cancer is lower than that of some common cancers, it has a lower average five-year survival rate. The average five-year survival rate for oral cancer is 62%, compared to 89% of breast cancer, 99% of prostate cancer and 64% of colorectal cancer [2]. However, when detected in its early stage, the five-year survival rate for oral cancer can be improved to 82% [3]. Thus, early detection is crucial.

The late diagnosis of oral cancer can be mainly attributed to the conventional clinical diagnosis method, which is based on visual inspection and palpation by the clinician, followed by one or more tissue biopsies for histopathological diagnosis. This conventional method has some disadvantages. On one hand, premalignant lesions are often undistinguishable from benign tissue by visual examination, making it difficult for early premalignant detection. On the other hand, since only a few biopsies can be taken, sampling errors introduced by the clinicians on choosing the most severe region to present the whole lesion is subjective to their experience and will ultimately decrease the diagnosis sensitivity.

The motivation of this study is to design an objective and reliable screening tool to help detect oral cancer in an early stage and guide tissue biopsy to avoid underdiagnosis and improve diagnosis yield.

Various optical imaging techniques are being explored for noninvasively detecting epithelial cancers *in vivo* due to their specific abilities to exploit tissue contrast mechanisms, which is called “optical biopsy”. However, most of these optical imaging systems are typically designed to either have a macroscopic view, sacrificing spatial resolution, or to have a high resolution with a limited field of view (FOV).

The ideal optical system to help detect carcinoma should have two main capabilities: First, the system should be able to conduct multi-scale imaging which is macroscopic surveillance guiding high resolution imaging. Second, since there are both biochemical and morphological changes during the progression of dysplasia, the system should also be able to characterize these changes as the diagnosis criteria.

To meet these requirements, a multimodal optical system was designed and built by our group. The system combined large-field fluorescence lifetime imaging microscopy (FLIM) and high-resolution reflectance confocal microscopy (RCM). It performs fast macroscopic FLIM surveillance, followed by depth sensitive, high resolution RCM imaging for suspicious locations manifested by FLIM. Since FLIM can provide information about tissue metabolism and biochemistry based on fluorescence as a source of contrast and RCM can detect morphologic changes based on the reflectivity difference between cell cytoplasm and nucleus as a source of contrast, we hypothesize that the comprehensive information provided by the combined system will increase the diagnosis accuracy of oral cancer in its early stage.

1.2 Objectives and dissertation organization

Although the overall aim of this project is to design and build a combined FLIM-RCM system, the objective for this dissertation is focused on designing, building and validating the FLIM subsystem for the combined FLIM-RCM system. Only one chapter in this dissertation describes the combined FLIM-RCM system on a bench-top form. The following endoscope systems are for FLIM subsystem only.

In order to build the FLIM subsystem for oral mucosa imaging *in vivo*, four major milestones were achieved.

First, a bench-top multispectral FLIM system was built to combine with RCM system with a translation stage for image co-registration. A preclinical trial on the hamster cheek pouch model of oral carcinogenesis was conducted.

Second, a flexible FLIM endoscope based on a wide-field time-gated implementation was built. The system was validated by the hamster cheek pouch model of oral carcinogenesis.

Third, in order to achieve faster imaging speed and more accurate lifetime estimation, a rigid handheld multispectral FLIM endoscope was built based on the pulse sampling implementation. The clinical study of human oral tissue was conducted *ex vivo* and *in vivo*.

Fourth, based on the feedback from the physicians who used the system, a compact version of the handheld endoscope with smaller size and less weight was built.

The chapters of this dissertation are organized according to the four milestones mentioned above:

In the introduction chapter, the motivation of this study and the organization of the dissertation are presented.

In Chapter 2, Section 2.1 introduces the concepts of fluorescence and fluorescence lifetime. Section 2.2 introduces the interested autoflorophores in epithelium and connective tissue and their changes associated with dysplasia. Section 2.3 introduces the three main implementations to conduct time-domain FLIM. Section 2.4 is a review of previously published FLIM endoscopes.

Chapter 3 focuses on the bench-top combined FLIM-RCM system. The design of the system is described in Section 3.1. Validation results of phantom imaging, porcine buccal mucosa imaging *ex vivo* and hamster cheek pouch imaging *in vivo* are presented in Section 3.2, 3.3 and 3.4, respectively. Section 3.5 and 3.6 are conclusion and discussion.

Chapter 4 focuses on the fiber-bundle based FLIM endoscope. The design of the system is described in Section 4.1. Validation results of standard dyes and hamster cheek pouch imaging *in vivo* are presented in Section 4.2 and 4.3, respectively. At last, the limitations of this system are discussed in detail in Section 4.4 which is the reason for designing the rigid handheld FLIM endoscope in Chapter 5 and Chapter 6.

Chapter 5 focuses on rigid handheld FLIM endoscope. The design of the system is described in Section 5.1. Validation results of standard dyes imaging, normal hamster cheek pouch imaging *in vivo* and normal human oral mucosa imaging *in vivo* are presented in Section 5.2, 5.3 and 5.4, respectively. In Section 5.5 and 5.6, results of oral biopsy imaging *ex vivo* and human oral cancer imaging *in vivo* are presented, respectively.

Chapter 6 focuses on the compact version of rigid handheld FLIM endoscope which might serve as the clinical prototype for *in vivo* study in the future. The design of the system is described in Section 6.1. Section 6.2, 6.3 and 6.4 present the results of standard dye validation, normal human oral mucosa imaging *in vivo* and oral biopsy imaging *ex vivo*, respectively.

In Chapter 7, a conclusion is made in Section 7.1. The discussion of the future work is presented in Section 7.2.

2. FLUORESCENCE LIFETIME IMAGING MICROSCOPY (FLIM)

2.1 Fluorescence and fluorescence lifetime

Fluorescence is the emission of light by a molecule which absorbs light or other electromagnetic radiation [4]. The absorption of light excites the molecule from its ground state to a higher energy state, and its return to the ground state gives rise to fluorescence emission. A simplified Jablonski diagram which only consists of two electronic states is shown in Fig.1 to demonstrate the generation of fluorescence, in which the ground state is labeled as S_0 and the first excited electronic state is labeled as S_1. In each state, several lines are drawn to represent the vibrational energy states within S_0 and S_1, respectively. Absorption happens when the energy of excitation matches the energy difference between the lowest vibrational state of S_0 and any of the vibrational states of S_1. Since there are several vibrational states within S_1, the absorption spectrum is broad. Likewise, the energy of emission equals the difference between lowest vibrational state of S_1 and any of the vibrational state of S_0, resulting in a broad emission spectrum. Because of the vibrational relaxation which is a non-radiative process among the vibrational states within S_1, the emission light has a longer wavelength than that of the excitation.

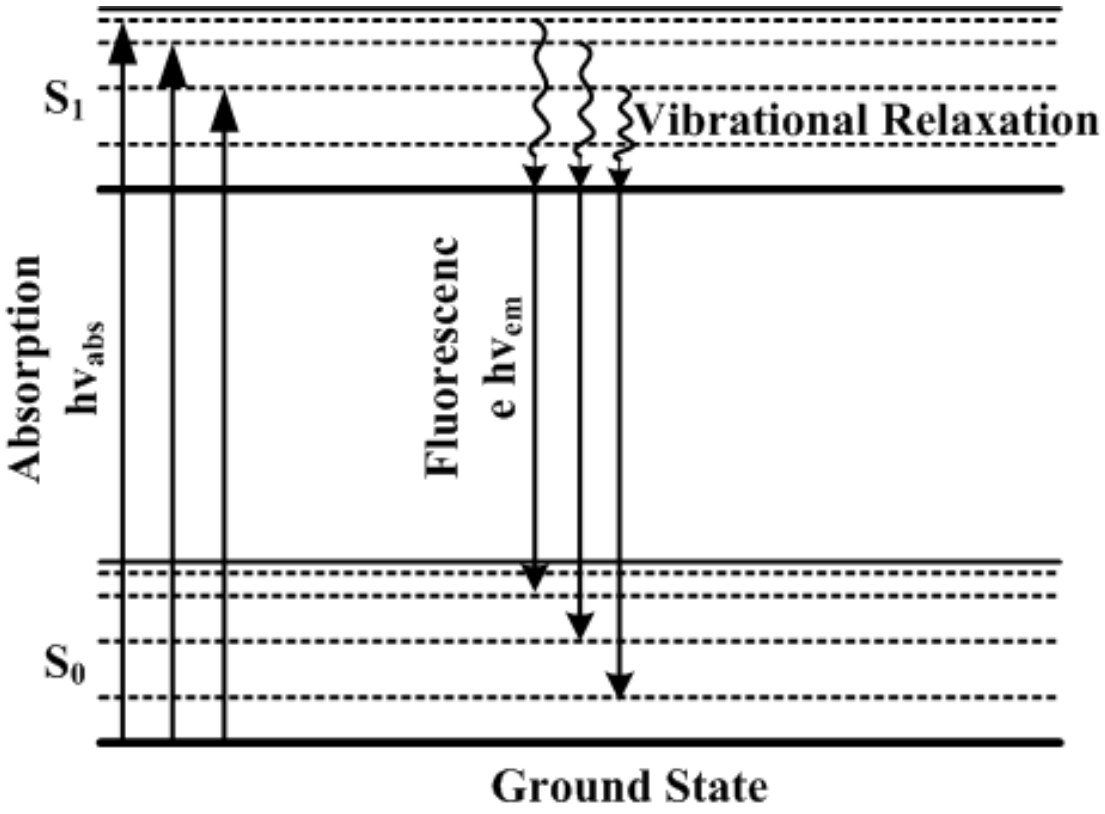

Figure 1: Simplified Jablonski diagram illustrating the various electronic and vibrational states of a molecule and the transitions between states. S_0: ground state, S_1: excited state.

Fluorescence lifetime is defined as the average time the molecule spends in the excited state prior to returning to the ground state [4]. The simplest case of a fluorescence decay follows a mono-exponential function. In this situation, the lifetime, denoted by τ in Eq. 2.1, is the time when the emission drops to 37% of the maximum intensity value I_0.

$$I(t) = I_0 e^{-t/\tau} \tag{2.1}$$

For more complicated samples that have several fluorescent components or follow the multi-exponential decay, an average lifetime can be calculated as in Eq. 2.2.

$$\tau = \frac{\int_0^\infty t\, I(t)dt}{\int_0^\infty I(t)dt} \tag{2.2}$$

2.2 Intrinsic autoflorophores in oral epithelial tissue

Autofluorophores in biological tissue have been of particular interest in clinical research studies. They can serve as label-free indicators of changes associated with dysplasia without the administration of contrast agents. In oral epithelial tissue, there are two layers which are divided by the basement membrane: the epithelium layer and underlying stroma layer. In the epithelium layer, there are metabolic coenzymes nicotinamide adenine dinucleotide (NADH) and flavin adenine dinucleotide (FAD) inside the living cells. In stroma layer, there are collagens and collagen crosslinks. During the progression of dysplasia, the morphological and biochemical changes, such as the increasing epithelium thickness and metabolism activity, will modulate the tissue autofluorescence emission. Increased fluorescence from epithelium due to the increased cellular metabolism and decreased fluorescence from stroma due to the breakdown of collagen crosslinks, infiltration of lymphocytes, and increased epithelial thickness are expected.

2.3 Methods of conducting the time-domain FLIM

Fluorescence measurements can be classified into two categories: steady-state and time-resolved. The steady-state method usually measures the absolute fluorescence intensity or the emission spectrum. Compared to time-resolved measurement, it can be achieved by a relative simple implementation and cheaper instrumentation. However, in biological tissue study, the overlap of the emission spectrums from different autofluorophores makes it difficult to resolve individual autofluorophores from the steady-state data. Also, steady-state method can be easily affected by some external factors during

in vivo imaging, such as the changes in light excitation-collection geometries, presence of endogenous absorbers, intensity artifacts caused by variation in tissue surface profile, and photobleaching effects [5]. The alternative method, time-resolved or lifetime measurement, can address those problems by resolving the sample's fluorescence decay dynamics. Since the lifetime of fluorophore is independent of fluorescence intensity, it is more robust for the clinical applications.

The time-resolved measurement can be performed in either time domain or frequency domain. As shown in Fig. 2 (a), in the time-domain measurement, the sample is excited by a short pulse of excitation and the emission decay is recorded as a function of time for lifetime calculation. In frequency-domain measurement as shown in Fig. 2 (b), the sample is excited with intensity modulated light at high frequency. The detected fluorescence emission is intensity modulated at the same frequency with a phase shift and a decreased modulation depth. The lifetime can be computed by the equations shown in Fig. 2 (b). For complex samples which have several lifetime components, different excitation modulation frequencies are required to cover the entire fluorescent decay dynamics.

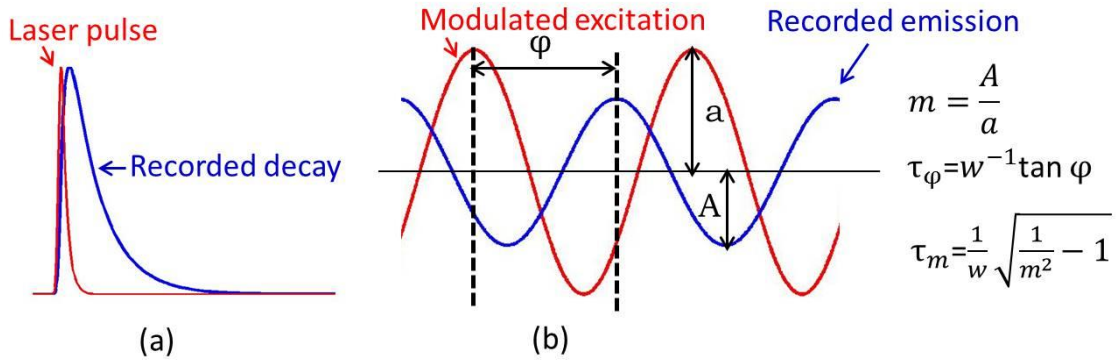

Figure 2: Time-resolved measurement techniques. (a) Time-domain FLIM is performed by exciting the sample with a short light pulse and the fluorescence decay is used for lifetime calculation. (b) Frequency-domain FLIM is performed by exciting the sample with an intensity modulated light source (sinusoidal signal with angular frequency ω as an example in the figure). The recorded emission signal with phase shift φ and intensity modulation m with respect to the excitation signal is used for lifetime calculation. τ_φ and τ_m are the two lifetimes.

In this dissertation, all the FLIM systems were built based on the time-domain measurement. There are three common implementations for time-domain FLIM: time-correlated single-photon counting (TCSPC), time-gated detection and pulse sampling [5].

In the TCSPC, a fluorescence decay curve is built as a histogram of the arrival time of the first detected photon after each excitation pulse as shown in Fig. 3 (a). At each spatial position (pixel), lots of photons are required to build up the histogram. It is recommended that 100 and 10,000 photons are needed to get a lifetime estimation accuracy of 10% and 1%, respectively. The pixel rate is determined by photon counting rate (typically a few MHz, smaller than laser repetition rate of tens of MHz) and total photon count per decay which is determined by the requirement for lifetime estimation accuracy. To give an example, if 10% lifetime accuracy is acceptable, a frame rate of ~0.6 Hz can be achieved for a 128 × 128 pixels image at 10^6 photon counting rate. The

advantages of the TCSPC include low required pulse energy, free of gain noise and high temporal resolution [6]. These advantages make the TCSPC technique ideal to detect minor lifetime changes in live cell study, e.g. forster resonance energy transfer (FRET) between molecules.

For time-gated implementation, the imaging is usually accomplished in wide field by a gated intensified charge coupled device (ICCD) as shown in Fig.3 (b). The gate of the ICCD opens at specific time to detect the fluorescence intensity. During imaging, a sequence of fluorescence intensity images is recorded at specific delays relative to the excitation pulse. The fluorescence decay curve for each spatial location is reconstructed by the multiple gates in the order of delay time. Since the imaging is in wide field and does not require scanning mechanism, it is simple for endoscopy implementation and save the time for scanning. However, there are several disadvantages. First, since the excitation pulse energy is distributed across the whole FOV, summing and averaging is necessary to achieve adequate signal to noise ratio (SNR). Second, in order to achieve higher temporal resolution, multiple gates are required to accurately reconstruct a decay curve, which will cause longer data acquisition time. Another disadvantage is this method is extremely sensitive to motion artifact. The sample cannot be moved during imaging in order to correctly reconstruct the fluorescence decay for each spatial position.

Pulse sampling is the most straightforward time-domain FLIM implementation. As shown in Fig. 3 (c), it directly records the fluorescence temporal decay after each excitation pulse using high-speed detectors and digitizers. If the pulse energy is high

enough to get a decent SNR, only one laser pulse is required for each pixel. Thus, the pixel rate equals to the laser repetition rate. By 2-D scanning the sample, an image is achieved.

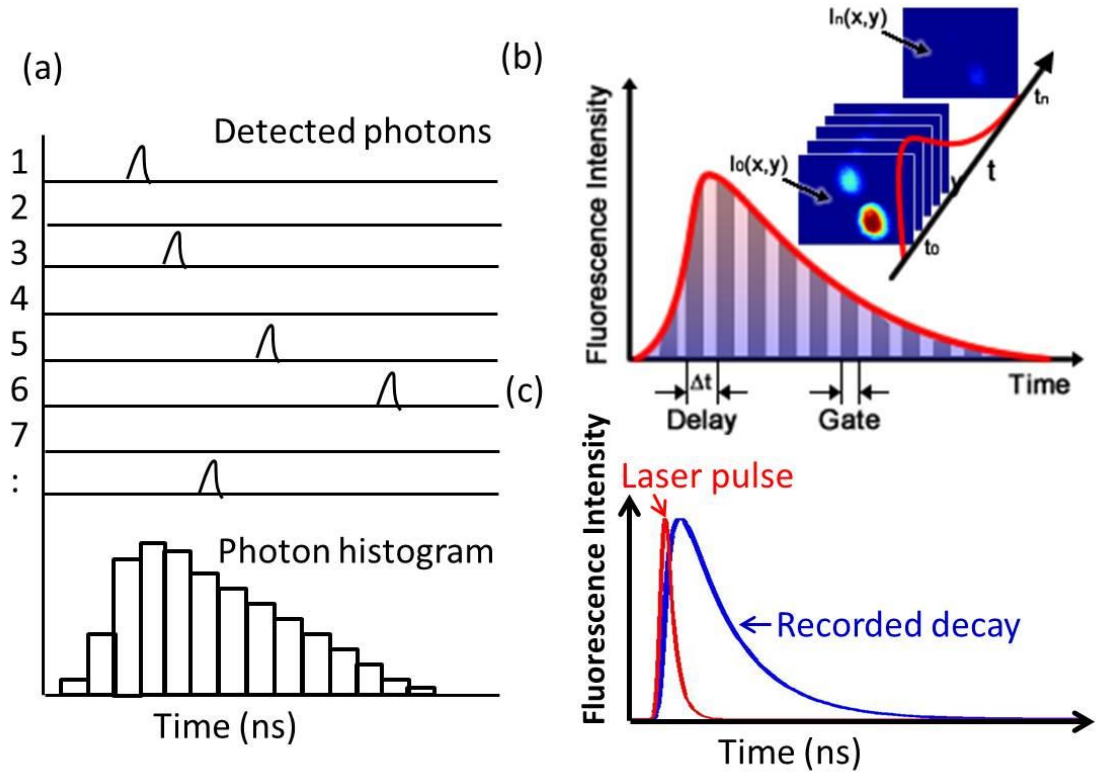

Figure 3: Time-domain FLIM implementations. (a) TCSPC, the decay curve is established as a histogram of the arrival time of the first detected photon for each laser pulse. (b) Time-gated detection with an ICCD, a sequence of fluorescence images (from I_0 (x, y) to I_n (x, y)) are captured with different delays (multiple times of Δt) with respect to the laser pulse. The gate labeled in the figure is the integration time for each image (c) Pulse sampling, the decay is recorded by fast detector (e.g. MCP-PMT).

2.4 Review of previous FLIM endoscopes for *in vivo* applications

Many FLIM endoscope designs have already been proposed. Wide-field FLIM endoscopy was first demonstrated in the frequency domain [7]. It had a limited spatial resolution of 32 × 32 pixels and was validated on human healthy mucosa of the bronchi *in*

vivo. With the development of the gated optical intensifier (GOI), several time-gated FLIM endoscopes in time-domain were demonstrated. J. Requejo-Isidro *et al*. built a rigid endoscope with a frame rate of 7.2 Hz. It was validated on a bisected lamb kidney *ex vivo* [8]. I. Munro *et al*. built a flexible endoscope with a frame rate of 5.5 Hz. The system was validated on fresh human stomach and lamb's kidney tissue *ex vivo* [9]. G. T. Kennedy *et al*. built a hand-held FLIM system based on a rigid clinical arthroscope and a custom-built GOI [10]. Recently, a flexible FLIM endoscope utilizing blue excitation light was demonstrated [11]. Compared to UV light, the blue excitation has the advantages of less concern on phototoxicity and less unwanted background fluorescence from the optical components. However, blue light cannot efficiently excite NADH, which is a very important autofluorophore for cancer detection. Besides the designs based on the time-gated implementation, two flexible endoscopes have been proposed using the TCSPC module [12, 13]. Both of them were applied to measure FRET in the live cells and were limited to visible wavelength excitation, restricting their use to exogenous fluorescence imaging. A common limitation of all these designs mentioned above, however, was the acquisition of the fluorescence emission was at a single emission band. Since the autofluorophores in biological tissue have distinguished spectrums, multispectral imaging will help resolve different autofluorophores.

For the multispectral FLIM endoscopy, one flexible endoscope design based on a wide-field time-gated implementation was proposed. The endoscope design was built around a flexible imaging fiber bundle, multispectral imaging was realized by placing a filter wheel in the emission optical path, and illumination was delivered using an adjacent

multimode fiber [14]. This endoscope was recently used to image oral cancer and brain cancer *in vivo* [15, 16]. However, this design presented three main limitations. First, since multispectral imaging was sequential, the time required to record FLIM images at multiple emission bands increased with the number of spectral bands. Second, since illumination light was delivered through a fiber adjacent to the imaging bundle, achieving uniform illumination and endoscope compactness could be challenging. Third, like all the wide-field time-gated FLIM, in order to achieve a fast imaging speed, a rapid lifetime determination (RLD) algorithm had to be adopted which limited the temporal resolution. This trade-off between temporal resolution and imaging speed was overcome by several FLIM systems based on the pulse sampling implementation stated below.

A multispectral FLIM catheter was designed and combined with ultrasound imaging for intravascular diagnosis [17, 18]. Due to the low repetition rate of the laser source (30 Hz), the imaging speed was slow. The upgrade version of this system was published later with a high repetition rate laser (1 MHz). The system was validated on a swine model of pig arteries *in vivo*. However, the average excitation power they used exceeded the maximum permission energy (MPE) set by ANSI, which made it not suitable for human *in vivo* imaging. A hyperspectral FLIM was proposed by Nie *et al*. [19]. The system was capable of performing time-resolved measurements at multiple emission wavelengths with high spectral resolution by means of an acousto-optic tunable filter (AOTF) which allowed rapid random wavelength switching in the collection path. The system was validated on porcine skin specimens *ex vivo*. However, the reported pixel rate was slow (~3 Hz). Yankelevich *et al*. reported a multispectral time-resolved fluorescence spectroscopy

(TRFS) system recently [20]. The imaging speed was 9.6s for 1500 pixel which is still not fast enough to avoid motion artifact for *in vivo* imaging. In addition, both systems in [19] and [20] were limited to one single point detection. The beam steering mechanism was not integrated, and imaging was achieved by an external stage to move the sample.

3. BENCH-TOP COMBINED FLIM-RCM SYSTEM*

3.1 Bench-top combined FLIM-RCM system

In order to determine specific design parameters for the endoscope system and characterize the system's performance for detecting oral precancer and cancer, a bench-top combined FLIM-RCM system was built before endoscope designs [21].

In the multi-scale multimodal FLIM-RCM system, FLIM is used to provide real-time macroscopic images of the biochemical makeup of the specimen. These images then serve as a guide to direct RCM to suspicious sites within the FOV. Co-registered RCM facilitates morphological imaging of the sub-cellular structure of the epithelium with small FOV, but very high spatial resolution in three dimensions. The greatest contrast source of RCM in the epithelium is the variation in tissue refractive index, for example, the cell nuclei compared to the surrounding cytoplasm [22]. This enables visualization of cell nuclei and quantification of the features such as the nuclear-to-cytoplasmic ratio. The nuclear-to-cytoplasmic ratio is one of the morphological features for diagnosis of oral epithelial dysplasia and oral squamous cell carcinoma [23].

The multimodal optical system is designed to probe the biochemical properties of tissue on a macroscopic scale and the cellular morphology with a high resolution. Therefore, a large-field FLIM and a high-resolution RCM subsystems are placed adjacently with a common sample translation stage for co-registration of images. A

* Reprinted with permission from "Fluorescence lifetime imaging and reflectance confocal microscopy for multiscale imaging of oral precancer" by Jabbour. J.M., Cheng S., Malik B.H., Cuenca R., Jo J.A., Wright J., Cheng Y-S.L., Maitland K.C., 2013. Journal of Biomedical Optics, 18(4), p. 046012, Copyright [2013] by Society of Photo-Optical Instrumentation Engineers.

detailed schematic of our integrated system is shown in Fig. 4. For FLIM subsystem, a frequency-tripled Q-switched ND: YAG laser (355 nm, <1ns pulse duration, 100 kHz maximum repetition rate, AOT-YVO-100QSP/MOPA, Advanced Optical Technology) was used as excitation. The laser light was coupled into a multimode fiber with a core diameter of 50 μm (FVP050055065, Polymicro Technologies) and delivered to the bench-top system. The output of the excitation fiber was collimated and then reflected by a dichroic mirror (DM1: NC176741-z355rdc, Chroma) to a pair of galvanometer mirror scanners (6200HM40, Cambridge Technology) for two-dimensional raster scanning. A UV-NIR corrected triplet (f=45mm, NT64-837, Edmunds Optics) was used to focus light in the sample. The fluorescence emission was collected by the same triplet and passed the dichroic mirror (DM1) to the collection fiber with a core diameter 200 μm (BFL22-200, Thorlabs). The output of the collection fiber was launched to a multispectral detection unit which consisted of dichroic mirrors (DM2: T>95%@439-647 nm, LM01-427-25, DM3: T>95%@492-950 nm, FF484-Fdi01, Semrock), bandpass filters (F1: FF01-390/40, F2: FF01-452/45, Semrock), a long pass filter (F3: FF01-496, Semrock) and three multimode fibers with lengths of 1m, 13m and 25m (BFL22-200, Thorlabs). The detection unit separated the fluorescence emission into three spectral bands which were selected based on emission spectrum of the three endogenous fluorophores of interest: collagen (F1: 390 ± 20 nm), NADH (F2: 452 ± 22.5 nm) and FAD (F3: >500 nm). The three multimode fibers with different lengths provided a time delay of 60ns with 12 meter length difference and helped temperately separate the signals from the three spectral bands. Therefore, for each laser pulse, three fluorescence decays for three spectral channels could be detected

simultaneously with one single detector. The outputs of the three fibers were then detected by a high-speed micro-channel plate photomultiplier tube (MCP-PMT, 180 ps rise time, 90 ps transit time spread, R5916U-50, Hamamatsu), amplified by a preamplifier (C5594-12, Hamamatsu) and sampled by a digitizer at 6.25 GHz (PXIe-5185, National Instruments) using custom software programmed in LabVIEW (National Instruments). The FLIM data was then processed with MATLAB (Mathworks, Natick, MA). For each sample, nine maps were generated: three absolute intensity maps (I_1, I_2 and I_3), three normalized intensity maps (I_{1n}, I_{2n} and I_{3n}) and three average lifetime maps (τ_1, τ_2 and τ_3) for three spectral channels, respectively. The I_1, I_2 and I_3 were the time-integrated intensity values at corresponding pixels in the 390 nm, 452 nm, and >500 nm spectral bands, respectively. The I_{1n}, I_{2n} and I_{3n} were calculated by $I_{1n}=I_1/(I_1+I_2+I_3)$, $I_{2n}=I_2/(I_1+I_2+I_3)$, $I_{3n}=I_3/(I_1+I_2+I_3)$ *to* show the proportion of each spectral channel among the three spectral channels. To calculate average lifetime, the measured fluorescence decays were first deconvolved from instrument response function (IRF) using the Laguerre deconvolution method to get real intrinsic fluorescence decays. The average lifetime τ_{ave} was then calculated from the intrinsic fluorescence decay $h(t)$ with $\tau_{ave} = \sum t \cdot h(t) / \sum h(t)$, where t is time.

This bench-top FLIM subsystem had a field of view (FOV) of 16×16 mm^2 while being able to distinguish element 1 of group 3 of USAF target corresponding to a lateral resolution of 62.5 μm using 400×400 pixels per image. For each pixel, only one pulse with a pulse energy of 1 μJ/pulse was used. The generated fluorescence signal had a decent signal to noise ratio (SNR) and no average was applied. As a result, the pixel rate was

equal to laser repetition rate. The acquisition of one single image took 19.2 s with 400×400 pixels at 10 KHz laser repetition rate. The frame rate was varied depending on the number of pixels per frame and the laser repetition rate. The temporal resolution was calculated to be 320 ps based on the Nyquist theorem with 6.25 GS/s sampling rate.

For the RCM subsystem, a near infrared (NIR) continuous wave diode-pumped solid state laser (1064 nm, 1 W, CL1064-1W0, Crystalaser, Reno, NV) was used as the illumination source. A combination of a half-wave plate and a linear polarizer in the beam path served as a variable attenuator to control the optical power incident on the sample. A spatial filter in the beam path was used to produce a clean Gaussian beam. An 8 kHz resonant scanner and a galvanometer scanner operating at 7 Hz (CRS 8K and 6215HM40, Cambridge Technology) were close-coupled to raster scan the NIR beam. A 2× beam expander filled the back aperture of a water immersion objective lens (60×, 1.0 NA, 2 mm working distance, LUMPLFLN60X/W, Olympus, Center Valley, PA), which focused the light onto the sample. A combination of linear polarizer, polarizing beam splitter, and quarter wave plate were used to remove specular reflections within the optical system. Finally, a spatial filter with a confocal pinhole of 30 μm diameter for optimized system characterization and 50 μm diameter for tissue imaging rejected the out of focus light prior to signal detection by an avalanche photodiode (APD) module (APD110C, Thorlabs).

The RCM subsystem was measured to have a 400 μm diameter FOV and a lateral resolution of 0.97 μm. The FWHM axial resolution was measured to be 3.5 μm and 4.5 μm using 30 μm and 50 μm diameter pinholes, respectively. The larger pinhole was used for imaging tissue samples in order to increase signal to noise ratio.

An automated translation stage was used to move the sample between the FOVs of the FLIM and the RCM subsystems which were approximately 90 mm apart. A 1951 positive USAF resolution target placed on a white paper was used to acquire co-registered images from the two subsystems with lateral accuracy less than the FLIM lateral resolution.

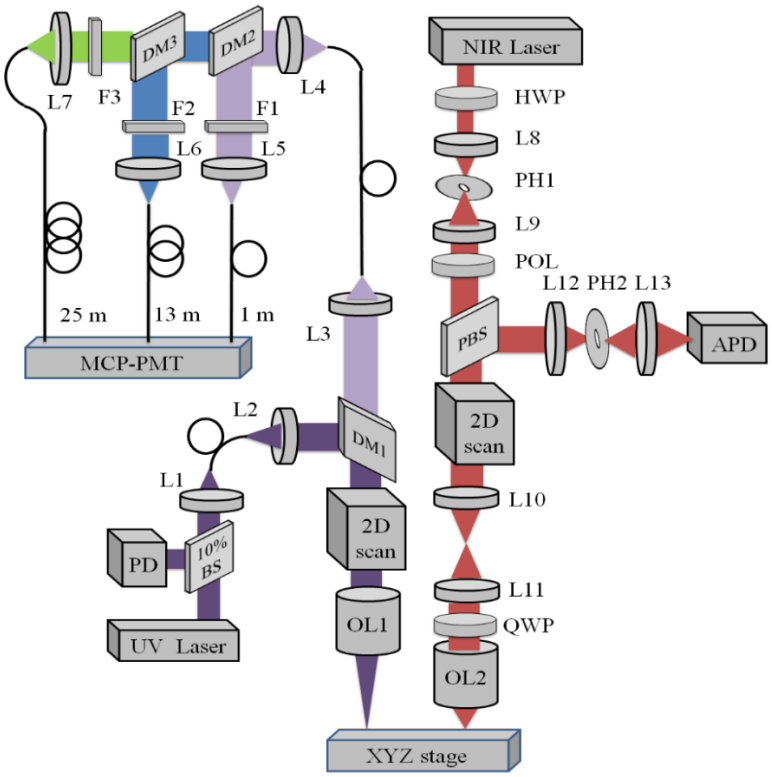

Figure 4: Schematic of the combined FLIM-RCM system. Left: FLIM subsystem. DM: Dichroic mirror, F: Filter, PD: Photodiode, BS: Beam splitter, L: Lens. OL: Objective lens. Right: RCM subsystem. PH: Pinholes, APD: Avalanche photodiode, HWP: Half wave plate, POL: Polarizer, QWP: Quarter wave plate, PBS: Polarizing beam splitter. An XYZ translation stage co-registers FLIM and RCM images.

3.2 Tissue phantom imaging

The first step to validate the system was tissue phantom imaging. A two-layer tissue phantom was developed to test the system's capability to detect the macroscopic biochemical and microscopic morphological properties of a relatively complex sample. The phantom was produced with a thin top layer of 100-120 μm consisting of polymer beads to model the epithelial nuclei. NADH and FAD (Sigma-Aldrich) were also added to the top layer to mimic autofluorescent metabolic coenzymes in the epithelium. The NADH powder was concentrated towards the center and FAD was uniformly distributed throughout this layer. The top layer was set on top of a thick lower layer of collagen matrix which represented of stroma layer. In order to get a homogenous collagen matrix, collagen solution (rat tail tendon type I collagen, BD Biosciences) was used instead of collagen fiber. The dissolved collagen solution was added to 10 × phosphate buffered saline (PBS) solution and 1 M sodium hydroxide (NaOH) along with deionized water. The solution was allowed to gel at 37^{o}C for 30 minutes. However, the collagen gel was later found to have minor fluorescence under 355nm which was our excitation wavelength. The tissue phantom samples were prepared in a 96-well plate. The diameter of the wells was measured to be ~7 mm. The FLIM FOV was adjusted accordingly to capture a single well within the image.

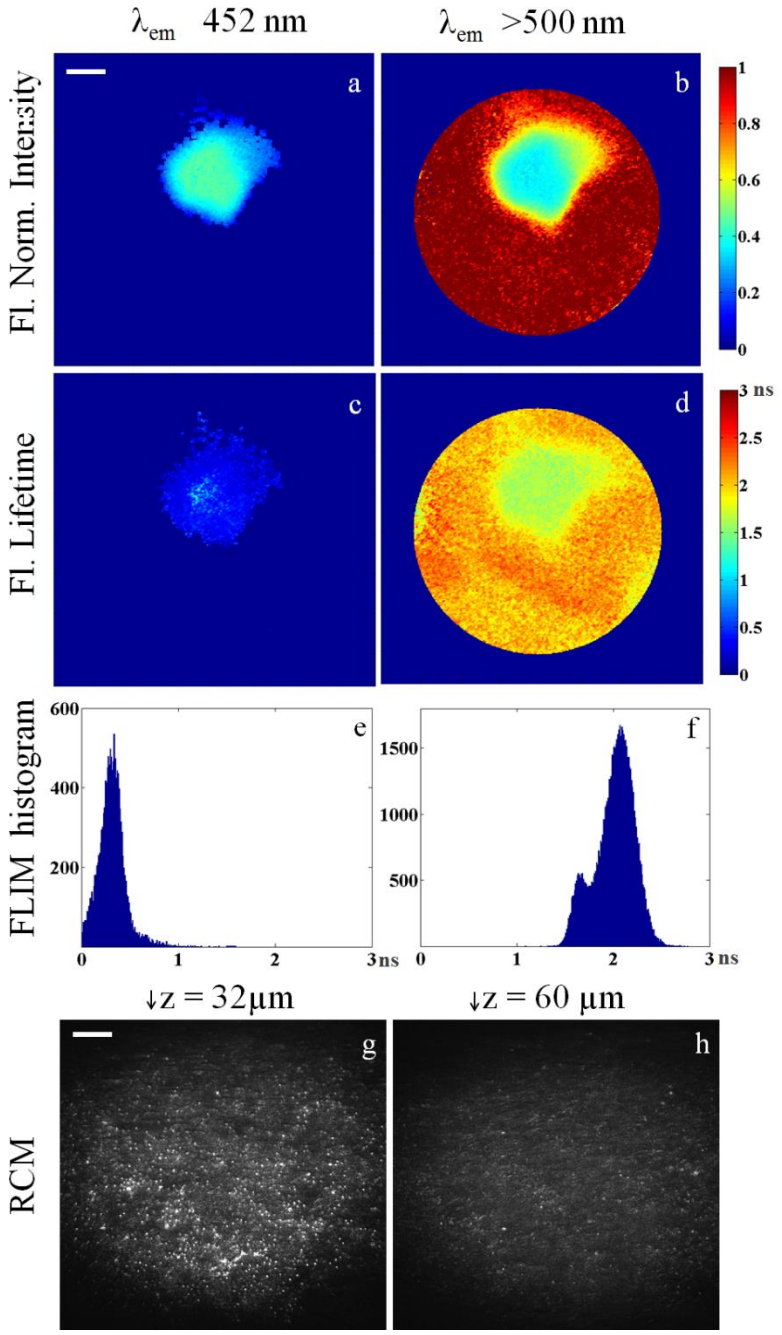

Figure 5: FLIM-RCM images of the two-layer phantom. FLIM normalized intensity maps at spectral channels of (a) 452±22.5 nm (b) >500 nm, and FLIM average lifetime maps and lifetime histograms at (c) and (e) 452±22.5 nm and (d) and (f) >500 nm, respectively. RCM images at (g) 32 μm and (h) 60 μm depths. Scale bar in (a) is 2 mm for FLIM and in (e) is 50 μm for RCM.

Fig. 5 shows the result of the phantom imaging. Since the collagen gel was found to be nearly non-fluorescent at 355 nm excitation, the signal in the 390 nm channel is less than 5% relative to the 452 nm and >500 nm channels. Therefore, images are shown only for the 452 nm (Fig. 5 (a) and (c)) and >500 nm (Fig. 5 (b) and (d)) bands corresponding to NADH and FAD emission, respectively. The circular mask shown in Figs. 5 (a) - (d) is the boundary of the phantom well in the 96-well plate. At 355nm excitation, peak emission wavelengths for NADH and FAD are around 450 nm and 520 nm, respectively. Part of the NADH fluorescence signal may be detected in the FAD band, whereas FAD fluorescence is limited to the >500 nm band. Fig. 5 (a) and (b) show FLIM normalized intensity maps at 452 nm and >500 nm bnads. The center of the phantom, where both NADH and FAD are present, provides fluorescence signal in both spectral channels (0.48 $\pm$0.08 a.u. in 452 nm band, and 0.45 $\pm$0.08 a.u. in >500 nm band). At the periphery of the phantom, the overall signal is dominated by FAD fluorescence in the >500 nm spectral channel (0.88 $\pm$0.09 a.u.). The known average lifetimes for unbound NADH and FAD are approximately 0.5 ns and 2 – 2.5 ns, respectively [24]. Fig. 5 (c) and (d) are the average lifetime maps, and Fig. 5 (e) and (f) are the corresponding lifetime histograms. As shown in the figures, the average lifetime for the center of the phantom in the 452 nm channel is 0.32 $\pm$0.15 ns corresponding to the lifetime of unbound NADH. The average lifetime in the >500 nm channel is 2.08 $\pm$0.15 ns at the periphery which represents FAD, and 1.72 $\pm$ 0.14 ns in the center which is the lifetime combination of NADH and FAD. Fig. 5(g) and 5(h) show the confocal images from the top-layer of the tissue phantom at depths of approximately 30 μm and 60 μm, respectively. The polystyrene beads appear as white

dots in the reflectance images, and are fairly uniformly distributed over the entire FOV. These results demonstrate that such a two-layer phantom is well-suited to validate our dual-modality imaging system.

3.3 Porcine buccal mucosa imaging *ex vivo*

Porcine buccal mucosa was used as a model of human oral mucosa due to their similar epithelial thickness. Healthy porcine tissue was obtained from a local slaughterhouse or through the tissue sharing program at Texas A&M University, and transported to the lab for imaging within a couple of hours postmortem. 2×2.5 cm^2 buccal mucosa tissue samples were excised from the inner cheek and placed in PBS solution prior to imaging. The pig tissue was at room temperature (~70 ℉) during imaging.

Fig. 6 shows the result of the porcine buccal mucosa imaging *ex vivo*. The normalized intensity maps (Fig. 6 (a) - (c)) indicates slightly stronger fluorescence signal in the 452 nm band (0.42 ± 0.02 a.u.), followed by the >500 nm band (0.31 ± 0.03 a.u.) and 390 nm band (0.27 ± 0.02 a.u.). The weak signal in the collagen channel (390nm channel) may be due to the thick epithelium, which makes it difficult for the fluorescence from collagen to reach the surface of the tissue. The thickness of the epithelium is more than 400 μm as shown in the H&E histology images in Fig. 6 (j). The average lifetime images (Fig. 6 (d) - (f)) show relatively longer values at 390 nm (5.84 ± 0.49 ns), followed by >500 nm (5.09 ± 0.41ns) and 452 nm (4.26 ± 0.41 ns) channels. Both intensity and lifetime maps are homogeneous, as expected in normal tissue. The RCM images in Fig. 6 (g)-(i) clearly shows the epithelial cell nuclei as bright spots on a darker background. Both the nuclear

density and nuclear-to-cytoplasmic ratio increase with depth in the epithelium, which is a hallmark of normal epithelium.

3.4 Preclinical *in vivo* imaging of a hamster cheek pouch model of oral cancer

The hamster cheek pouch model of oral cancer was employed to evaluate the system's performance to differentiate dysplasia from normal tissue. Specifically, the hamster was imaged during the early stages of 7,12-dimethylbenz [α] anthracene (DMBA)-induced oral carcinogenesis. A Golden Syrian hamster was used in this study. The animal use protocol was reviewed and approved by the Texas A&M University Institutional Animal Care and Use Committee (IACUC), and a veterinarian oversaw the clinical aspects of this study. The hamster was housed in pathogen-free conditions and fed with rodent chew and water *ad libitum*. The right buccal pouch of the hamster was treated 3 times a week for 8 weeks with 0.5% solution of DMBA (Sigma-Aldrich) dissolved in mineral oil (Sigma-Aldrich). The left pouch was treated with mineral oil only and served as a normal control. At the time of imaging, the hamster was anesthetized using an intraperitoneal injection of 10% urethane solution. Once anesthetized, the hamster cheek pouch was pulled and clamped into a custom built mount to expose maximum tissue area. During the imaging procedure, the anesthetized hamster was kept warm with a heating pad. The exposed cheek pouch was likely between room temperature and body temperature of the hamster. After imaging of the buccal mucosa, the hamster was euthanized with a solution of pentobarbital. The cheek pouches were then excised, fixed in 10% formalin, and processed for H&E histology.

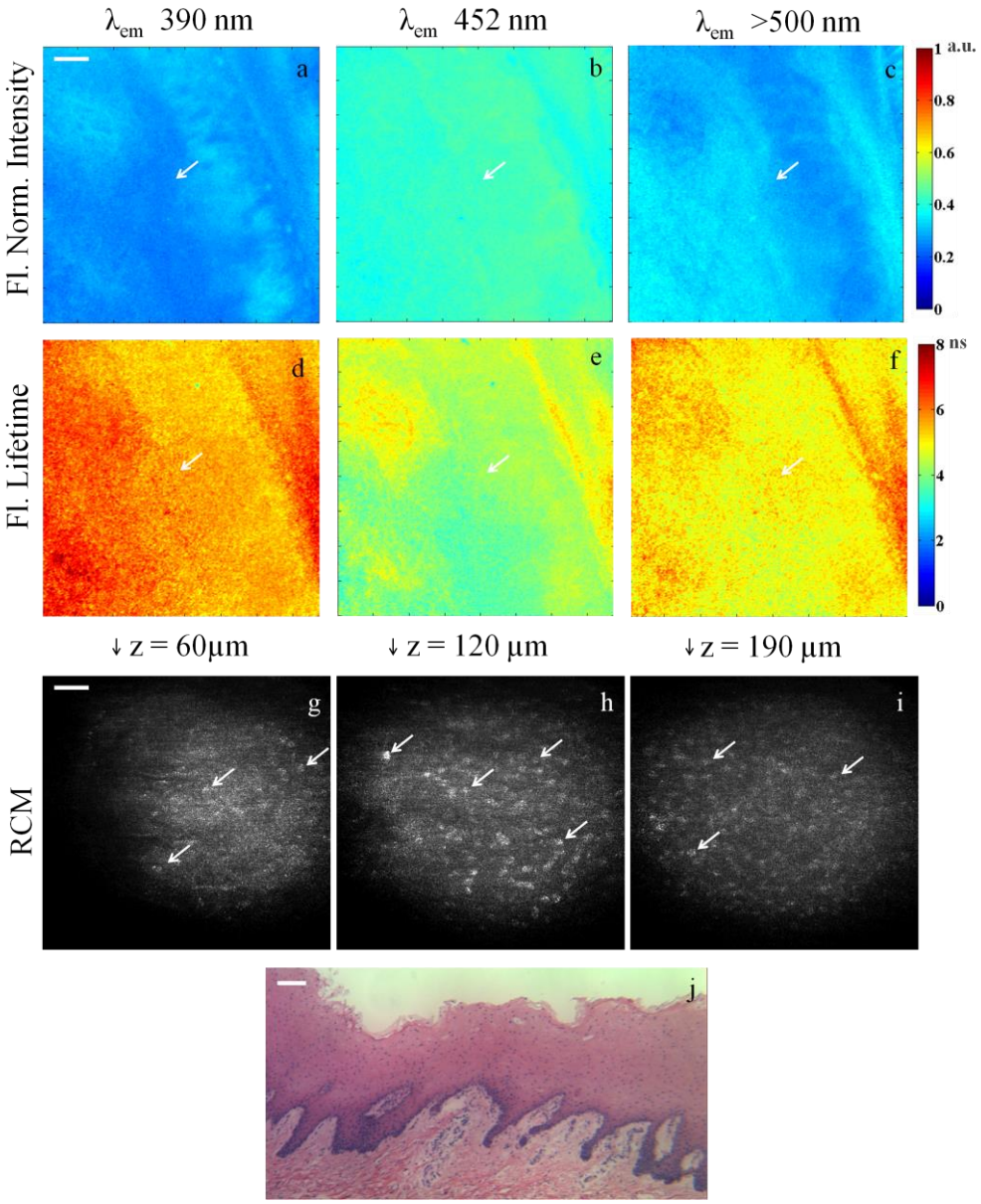

Figure 6: *Ex vivo* FLIM-RCM images of the normal porcine buccal mucosa. Normalized intensity maps at (a) 390 ±20nm, (b) 452 ±22.5nm, and (c) >500 nm. FLIM average lifetime maps at (d) 390 ±20nm, (e) 452 ±22.5nm, and (f) >500 nm. Arrows in (a) - (f) identify the RCM imaging location at the center of the FLIM FOV. RCM images obtained at (g) 60 µm, (h) 120 µm, and (i) 190 µm depths. Arrows in (g) - (i) point to individual nuclei. (j) 10 × H&E histology image of tissue. Scale bar is 2 mm in (a), 50 µm in (g), and 100 µm in (j).

Fig. 7 and Fig. 8 show the results for the normal and the DMBA-treated hamster cheek pouch, respectively. Fig. 7 (a)-(f) show the normalized fluorescence intensity and average lifetime maps for the normal hamster cheek pouch. The normalized fluorescence intensity values are 0.42 ± 0.04 a.u., 0.3 ± 0.01 a.u., and 0.28 ± 0.03 a.u., and lifetimes values are 5.61 ± 0.13 ns, 4.06 ± 0.25 ns, and 4.22 ± 0.29 ns for the 390 nm, 452 nm, and >500 nm bands, respectively. These results are consistent with a dominant collagen fluorescence emission that peaks at 390 nm and has an average lifetime of 5-6 ns. This is expected for the normal hamster cheek pouch, since the epithelium is very thin as shown in Fig. 7 (k) and most of the autofluorescence emission should come from collagen in the connective tissue. In comparison to the weak collagen signal in the thick porcine buccal mucosa, the fluorescence intensity in the 390 nm band is relatively high in the hamster cheek pouch tissue due to the very thin epithelium. The RCM images taken from the center of the FLIM FOV at approximate depths of 18 μm (Fig. 7 (h)) and 39 μm (Fig. 7 (i)) show scattering from the keratin at the surface, and epithelial nuclei beneath this superficial layer. Fig. 7 (j) is a zoomed in view of Fig. 7 (i) to more clearly show the cell membranes and nuclei identified by arrows.

Fig. 8 (a)-(f) show the normalized fluorescence intensity and the average lifetime maps for the DMBA-treated hamster cheek pouch. As seen in the corresponding photograph of the tissue in Fig. 8 (g) and in the FLIM images, a tumor is visible in the lower right quadrant of the tissue. In each FLIM map, two locations are marked by arrows labeled as Region 1 and Region 2. Region 1 was later diagnosed as cytologic atypia as shown in Fig. 8 (h) and Region 2 was diagnosed as low-grade dysplasia as shown in Fig.

8 (i) by histopathology. In these lesions, the fluorescence lifetime in the 452 nm channel is shorter (4.32 ± 0.18 ns and 4.29 ± 0.29 ns in Regions 1 and 2, respectively) compared to the normal tissue (>5 ns). Since NADH has a much shorter fluorescence lifetime (~0.5 ns) and its peak emission is at 450 nm, the resulting fluorescence in the pre-cancerous lesions is expected to have shorter lifetimes at 452 nm than in normal tissue. In the tumor region, the epithelium is so thick that all the fluorescence contribution is coming from this layer. Since the collagen in the connective tissue is either deconstructed or no longer excited due to the increasing epithelial thickness, the signal at 390 nm is insignificant (0.06 ± 0.03 a.u.). Strong emission is observed at >500 nm (0.75 ± 0.14 a.u.) and significant emission is also observed at 452 nm (0.19 ± 0.11 a.u.) in the tumor region. The extremely low signal in 390 nm band in the tumor region results in inaccurate lifetime measurements; therefore, the lifetime map in Fig. 8 (d) is masked in this tumor region. The fluorescence lifetime at 452 nm is much shorter (2.62 ± 0.79 ns) compared to normal tissue indicating a greater fluorescence contribution from NADH. The fluorescence lifetime in the 500 nm channel is longer (5.62 ± 1.27 ns) compared to normal tissue indicating contribution of both FAD and porphyrin; porphryin has relatively long lifetime (>6 ns) [15]. The RCM images of Region 1 just below the surface (Fig. 8 (j)) and deeper in the epithelium (Fig. 8 (l) and Fig. 8 (m) zoomed in) show very small features that may be epithelial nuclei or possibly nucleoli that can be seen in the corresponding histology section in Fig. 8 (h). In contrast, the RCM images of the epithelium in Region 2, shown in Fig. 8 (n), 8 (m) and Fig. 8 (o) zoomed in, show much larger nuclei indicative of precancerous changes. Arrows in RCM images identify cell nuclei.

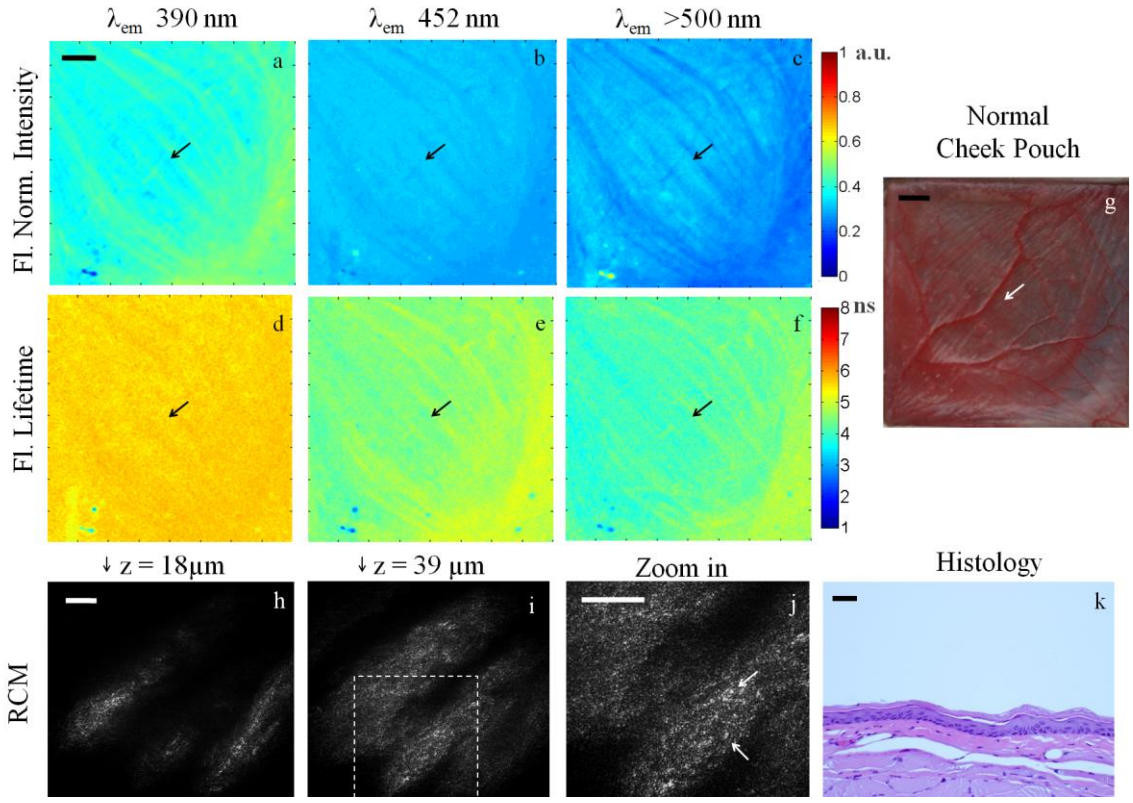

Figure 7: *In vivo* FLIM-RCM images of normal hamster cheek pouch. Normalized FLIM intensity maps at (a) 390 ±20nm, (b) 452 ±22.5nm, and (c) >500 nm. FLIM average lifetime maps at (d) 390 ±20nm, (e) 452 ±22.5nm, and (f) >500 nm. (g) Photograph of imaging areas. RCM images (h and i) taken at different depths below the surface. Zoom in RCM image (j) taken from dotted squares in (i). Arrows in RCM images point to individual nuclei. (k) 25 × H&E histology image. Scale bar is 2 mm in (a) and 50 µm in (k).

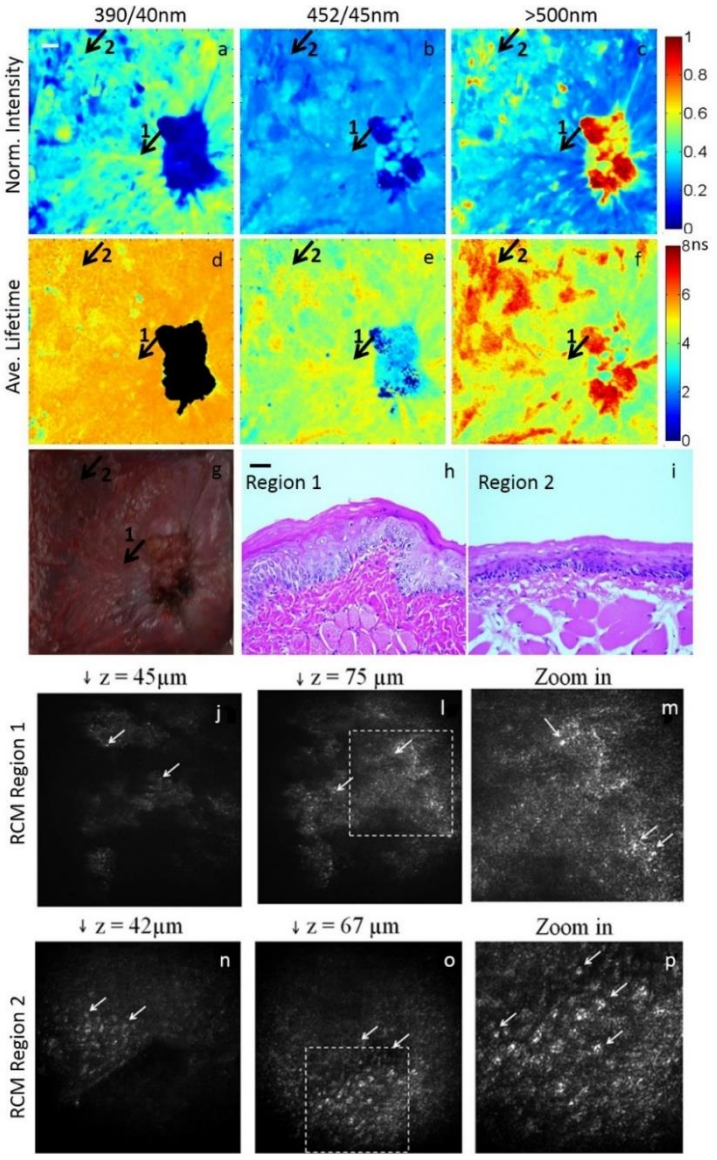

Figure 8: *In vivo* FLIM-RCM images of the DMBA-treated hamster cheek pouch. Normalized FLIM intensity maps at (a) 390±20nm, (b) 452±22.5nm, and (c) >500 nm. FLIM average lifetime maps at (d) 390±20nm, (e) 452±22.5nm, and (f) >500 nm. (g) Photograph of imaging areas. (h) and (i) 25× H&E histology images for region 1 (cytologic atypia) and region 2 (low-grade dysplasia), respectively. RCM images (j, l, n and o) taken at different depths below the surface. Arrows labeled 1 and 2 in the FLIM images in (a-f) correspond to regions for subsequent RCM images in (j-m) and (n-p), respectively. Zoom in RCM images (m and p) taken from dotted squares in (l and o) respectively. Arrows in RCM images point to individual nuclei. Scale bar is 2 mm in (a) and 50 µm in (h).

3.5 Discussion

This work shows that our dual-modality multispectral FLIM and RCM imaging system can effectively image biochemical and morphological features in tissue. While large-field FLIM enables fast macroscopic tissue evaluation, it lacks the ability to provide optical sectioning and high spatial resolution for cellular evaluation. The RCM subsystem can provide much higher spatial resolution and optical sectioning necessary for cellular imaging but has a limited FOV. The combination of these two imaging techniques on a single platform offers an important and powerful tool utilizing the strengths of the individual subsystems. The complementary information acquired from the integration of the two modalities is important for the study of biological changes such as those seen in the progression of early cancer.

In all instances, FLIM imaging provides macroscopic biochemical maps which represent the relative contribution of the endogenous fluorophores, both with respect to fluorescence intensity and lifetime. While the FLIM images of the tissue phantom show some physical features due to the geometry of the phantom and the distribution of NADH and FAD, the images of the biological samples showed differences in intensity and lifetime signals between normal and cancer. The FLIM maps of healthy pig mucosa are relatively homogeneous, as expected, due to the uniform nature of the normal tissue. The detected collagen signal from the pig mucosa with thick epithelium and the clear nuclei seen with RCM at different depths of tissue demonstrate the potential for translation to human oral tissue. Normal human oral mucosa, with an epithelial thickness ranging from 190 to 580 μm depending on the site in the oral cavity and cell nuclear diameters on the

order of 10 μm, has similar tissue architecture and cell morphology to pig oral mucosa [25]. In comparison, the hamster tissue has a wide range of pathologies, resulting in spatial features in both the intensity and lifetime images. Additionally, the spectral and lifetime data of the DMBA-treated pouch is different than the normal control pouch, indicating the ability to detect precancerous changes. By comparing the normalized intensity and average lifetime values in Table 1, differentiation between normal and tumorous tissue may be achieved with intensity measurements alone. However, based on some similarity in normalized intensity values and differences in lifetimes between normal tissue and the DMBA-treated RCM Regions 1 and 2, the more challenging and relevant problem of distinguishing between benign and precancerous lesions may be realized with FLIM. It should be noted that the histopathological difference between the normal and pre-cancerous lesions being compared are very subtle; yet, difference in the FLIM signal could already be observed. Nevertheless, the high resolution of RCM is still necessary for identifying cellular changes indicative of precancer.

The results from the high-resolution reflectance confocal microscope demonstrate the potential of the imaging system towards characterization of sub-cellular morphological features of the epithelial tissue. The brighter nuclei against the darker background can be delineated in the RCM images. The normal cell nuclei in the porcine tissue are on the same scale as the normal human epithelial cell nuclei. Although the normal hamster epithelial nuclei are smaller, they are still detectable with our RCM imaging system. An increase in nuclear size is distinguished between normal and dysplastic tissue in hamster cheek pouch. RCM images of the epithelial nuclei can be further analyzed either manually or through

automated image processing to calculate more objective parameters defining epithelial tissue characteristics such as nuclear size, nuclear density and nuclear-to-cytoplasmic ratio [26]. The RCM system was able to distinguish between two pathologically different regions that look similar using FLIM. This shows the importance of these two complementary techniques.

Table 1 Normalized fluorescence intensity and average lifetime for phantom, normal porcine mucosa, normal hamster cheek pouch and DMBA-treated hamster cheek pouch

Sample	λ_{em}	390 nm		452 nm		>500 nm	
		Intensity	Lifetime	Intensity	Lifetime	Intensity	Lifetime
Phantom	Center	--		0.48 ± 0.08	0.32 ± 0.15	0.45 ± 0.08	1.72 ± 0.14
	Outer	--		--		0.88 ± 0.09	2.08 ± 0.15
Normal Pig	Entire FOV	0.27 ± 0.02	5.84 ± 0.49	0.42 ± 0.02	4.26 ± 0.41	0.31 ± 0.03	5.09 ± 0.41
Normal Hamster	Entire FOV	0.42 ± 0.04	5.61 ± 0.13	0.30 ± 0.01	4.60 ± 0.25	0.28 ± 0.03	4.22 ± 0.29
DMBA-Treated Hamster	Tumor	0.06 ± 0.03	5.43 ± 0.14	0.19 ± 0.11	2.62 ± 0.79	0.75 ± 0.14	5.62 ± 1.27
	Region 1	0.49 ± 0.02	5.49 ± 0.16	0.28 ± 0.01	4.32 ± 0.18	0.23 ± 0.02	4.23 ± 0.21
	Region 2	0.42 ± 0.02	5.43 ± 0.14	0.27 ± 0.01	4.29 ± 0.29	0.30 ± 0.01	5.16 ± 0.34

3.6 Conclusion

In summary, we have presented the design and development of a dual-modality multi-scale bench-top FLIM-RCM imaging system applied to the characterization of oral epithelial tissue. The integrated system is capable of identifying both morphological features and the biochemical composition of mucosal tissue, which together can potentially serve as a powerful diagnostic aid towards classification of pathological condition of the tissue. Such a simultaneous characterization of tissue physiology may be

used to assess if the sample is normal, benign, premalignant or malignant, and may ultimately be used as a guiding tool for standard screening and intervention methods.

We are currently evaluating the system described here for differentiation of precancer from benign lesions in the hamster cheek pouch model. Following validation of this technology in an animal model and in human biopsies, the system can be miniaturized for *in vivo* imaging in humans using lens relays, fiber bundles, and miniature lenses.

4. FLEXIBLE MULTISPECTRAL FLIM ENDOSCOPE*

4.1 Flexible multispectral FLIM endoscope system

In order to translate the FLIM technique to the clinical arena, an endoscope or probe based design to access the oral cavity is required. To this effect, a compact FLIM endoscope based on fiber-bundle capable of simultaneous multispectral FLIM imaging at an imaging speed of ~2 fps was developed [27].

The system was built based on wide-field time-gated detection implementation. The system schematic is shown in Fig. 9. Since tissue endogenous fluorescence is best excited with UV light, a frequency-tripled Q-switched Nd:YAG laser was used as the excitation source (355nm, <1ns pulse duration, maximum repetition rate of 100KHz, AOT-YVO-100QSP/MOPA, Advanced Optical Technology). The endoscope was built around an imaging fiber bundle suitable for UV-VIS light transmission (10,000 elements, NA of 0.22, 1.1mm active area diameter, 1 m long, FIGR-10, Fujikura). A Lithium-based GRIN lens (Gradient Index lens, NA of 0.2, 1 mm diameter, GRINTECH) was placed at the distal end of the bundle with an air gap. Although the air gap gave rise to a loss of laser power from air-lens interface, it eliminated the background autofluorescence introduced by the glue which could corrupt the signal. A metal tube was used to connect the fiber bundle and the GRIN lens and to serve as a protective housing for the endoscope tip. The GRIN lens provided a working distance of 5 mm and a circular FOV of 2.25 mm in

* Reprinted with permission from "Flexible endoscope for continuous *in vivo* multispectral fluorescence lifetime imaging" by Cheng S., Rico-Jimenez J.J., Jabbour J., Malik B.H., Maitland K.C., Wright J., Cheng Y-S.L., Jo J.A., 2013. Optics Letters, 38(9), p. 1515-1517, Copyright [2014] by The Optical Society.

diameter (2.25 ×magnification). A dichroic mirror (DM1: NC176741-z355rdc, Chroma), placed at the proximal end of the imaging bundle, was used to reflect the laser beam into the fiber bundle and transmit the fluorescence emission to the detection arm. The laser beam size was allowed to be slightly larger than the active area of the bundle to achieve relative uniform illumination at the cost of coupling efficiency (~35%). The proposed endoscope design thus allowed both small diameter and uniform illumination.

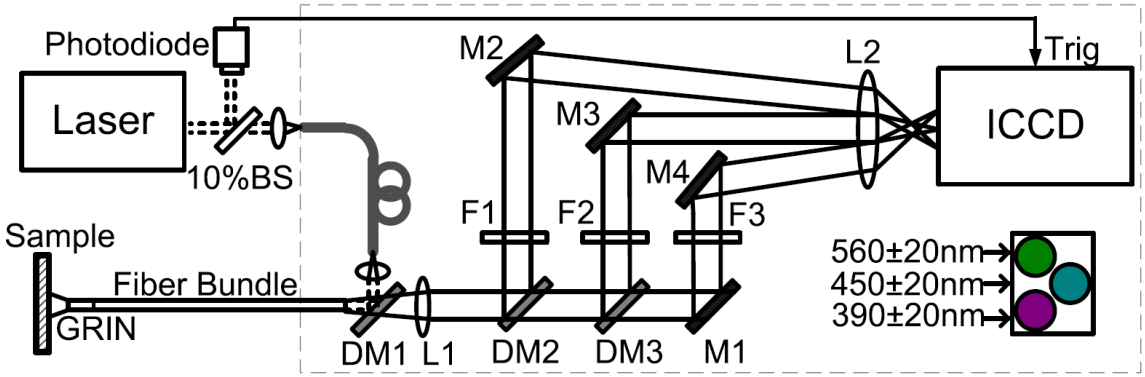

Figure 9: Schematic of the multispectral FLIM endoscope system. BS: Beam sampler, DM: Dichroic mirror, M: Mirror, F: Filter, L: Lens.

Wide-field time-gated FLIM was implemented using an intensified charge-coupled device (ICCD camera, 200-800 nm spectral range, 14.4 x 10.8 mm^2 active area, minimum 200 ps gate width, 33.8 Hz frame rate, 4Picos, Stanford Computer Optics). Simultaneous multispectral FLIM was implemented as follows: based on a similar approach previously proposed by Siegel *et al*. [28]. The fluorescence emission exiting the proximal end of fiber bundle was first collimated by an achromatic lens (L1: f=35 mm, Thorlabs). Then, a combination of two dichroic mirrors and one reflective mirror (DM2: T>95%@439-

647nm, DM3: T>95%@492-950nm, Semrock, M1: Ravg>97.5%@450-2000 nm, Thorlabs) with three band pass filters (F2: 390±20 nm, F3: 450±20 nm, F4: 560±20 nm, Semrock) were used to separate the fluorescence emission into three spectrally resolved collimated beams. Each beam was then directed and focused on different regions of the active area of the ICCD by means of three reflective mirrors (M2: Ravg>90% from 250 - 450 nm, M3-4: Ravg>97.5%@450-2000 nm, Thorlabs) and an achromatic lens (L2: f=150 mm, Thorlabs). The three spectral channels were selected based on the peak emission of three fluorophores of interest (collagen, NADH and FAD); however, they can be customized for a given specific application. The lateral resolution in all three spectral channels was measured to be ~35 μm by imaging a USAF resolution target (NT57-895, Edmund Optics).

The fluorescence lifetime maps were obtained by three methods: the rapid lifetime determination (RLD) with 2-gate protocol [29], the 4-gate protocol with a linearized least-squares lifetime determination method [30] and 20-gate method. The 2-gate protocol requires only two time-gated fluorescence images recorded at different delays with respect to the excitation pulse whereas the 4-gate and 20-gate methods require 4 and 20 time-gated images, respectively. The 2-gate and 4-gate methods treat the fluorescence decays as single exponentials, which is seldom the case for tissue autofluorescence. Nevertheless, the approximated average lifetime can still provide fluorescence lifetime contrast in biological tissue. The 2-gate method in our wide-field FLIM system allows an imaging speed of ~1 fps compared to ~0.5fps and ~0.1fps for 4-gate and 20-gate methods, respectively. Although in principle the frame rate for the 2-gate method should be faster

and equal to half of the frame rate of the ICCD (33.8 Hz), the time required to change the delays between gates at each consecutive frame is still too long (~500 ms) with the current control software of the ICCD.

4.2 Standard dyes validation

The FLIM endoscope was first validated with a set of three quartz capillary tubes loaded with 1 mM solutions of POPOP (in ethanol), NADH and FAD (both in PBS). The lifetime estimations from the three methods are listed in Table 2.

Table 2 Comparison of the lifetime estimation with 2-gate, 4-gate and 20-gate methods (unit: ns)

	390nm	450nm		560nm
	POPOP	NADH	POPOP	FAD
2-gate	0.93 ±0.21	0.51 ±0.06	1.07 ±0.24	2.32 ±0.56
4-gate	0.95 ±0.17	0.63 ±0.07	1.09 ±0.19	2.35 ±0.54
20-gate	1.50 ±0.11	0.55 ±0.07	1.60 ±0.20	2.49 ±0.11

As shown in Table 2, the 2-gate method provides smaller values than the 20-gate method, which is expected under the assumption that the fluorescence decays follow single exponential decays. However it does provide lifetime contrast among the three fluorescent dyes. Since the 4-gate and 20-gate methods take longer time and are not suitable for *in vivo* application, they were not adopted for the later studies in this chapter. In Fig. 10, the fluorescence intensity and average lifetime images from the three spectral channels with the 2-gate method are shown. As can be seen in Fig. 10 (a), strong emission

from POPOP is observed in both the 390±20 nm and 450±20 nm bands, while NADH and FAD emission is only observed in the 390±20 nm and 560±20nm bands, respectively. As shown in Fig. 10 (b), the average lifetime for POPOP, NADH, and FAD are estimated to be 1.07±0.24 ns, 0.51±0.06 ns, and 2.32±0.56 ns, respectively. The results from the three FLIM channels are in good agreement with the emission spectrums and lifetimes of the three fluorophores in literatures [24, 31, 32].

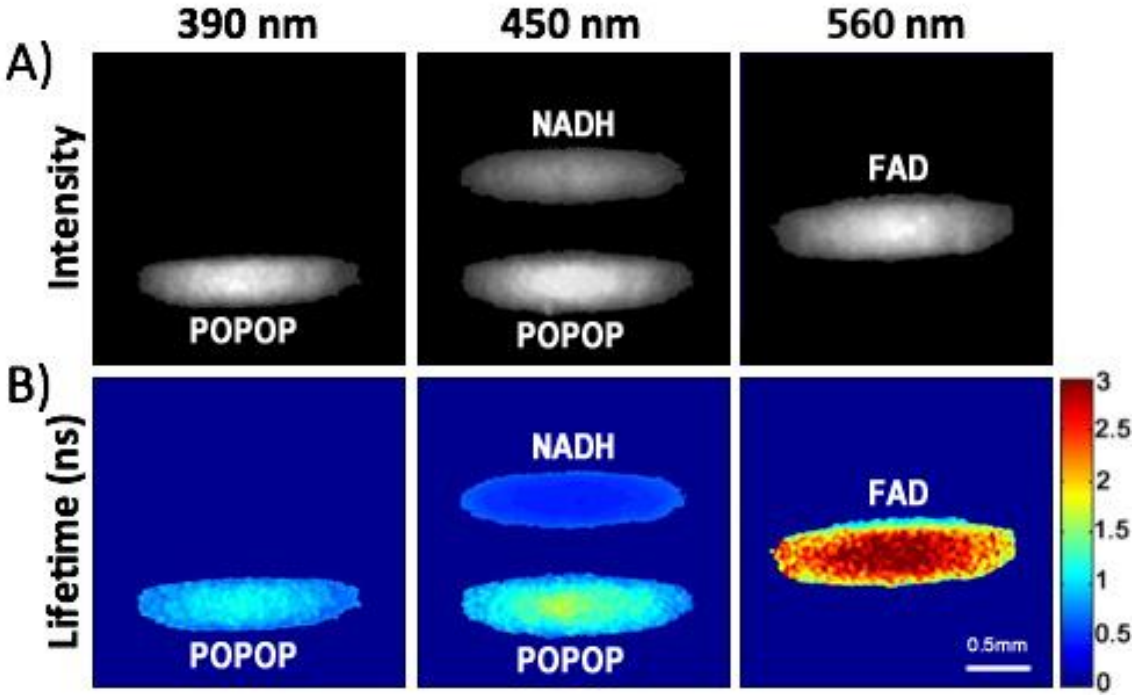

Figure 10: *In vitro* validation imaging of quartz capillaries loaded with (top to bottom) NADH, FAD, and POPOP. (A) Fluorescence intensity maps (B) Lifetime maps (colorscale in ns).

In order to demonstrate the system's potential for *in vivo* applications, continuous multispectral imaging was performed whereby two quartz capillary tubes loaded with 1 mM solutions of POPOP (in ethanol) and NADH (in PBS) were continuously imaged. A

total of ten consecutive fluorescence intensity and lifetime frames for the 450±20 nm channel are shown in Media 1 in the supplemental material. The lifetime maps clearly show longer lifetimes for the POPOP capillary (bottom) compared to the NADH capillary (top). To investigate the robustness of the imaging system to motion artifacts, the position of the capillaries was shifted at the 6th frame. While the intensity maps are not affected, the lifetime values are underestimated for part of the POPOP capillary during the shift in the capillary position; however, the lifetime maps are stabilized after one frame.

4.3 Preclinical *in vivo* imaging of a hamster cheek pouch model of oral cancer

The FLIM endoscope was further validated by imaging *in vivo* a lesion from a DMBA-treated hamster check pouch, which was diagnosed by histopathology as dysplasia. The imaging protocol for this study was approved by the Institutional Animal Care and Use Committee (IACUC) at Texas A&M University (TAMU). Multispectral FLIM images of the oral lesion surrounded by healthy tissue are displayed in Fig. 11, where it can be seen that the fluorescence intensity images have stronger fluorescence in the surrounding healthy tissue relative to the lesion area for all spectral channels. The fluorescence lifetime images for the 390±20 nm and 450±20 nm channels show longer values in the surrounding healthy tissue (~2-3 ns) relative to the lesion area (~1.2-1.6 ns), whereas for the 560±20nm channel, longer values in the lesion area (~1.6-1.7 ns) relative to the surrounding healthy tissue (~1.2-1.3 ns) can be seen. These fluorescence intensity and lifetime values in the lesion are similar to those of NADH and FAD, whereas the intensity and lifetime values of the surrounding healthy tissue suggest the presence of a

collagen rich area. These results are also consistent with the biochemical composition of normal and cancerous epithelial tissue.

Continuous multispectral FLIM imaging was also demonstrated *in vivo* on the same hamster cheek pouch lesion. A total of ten consecutive fluorescence intensity and lifetime frames for the three spectral channels are shown in Media 2 in the supplemental material.

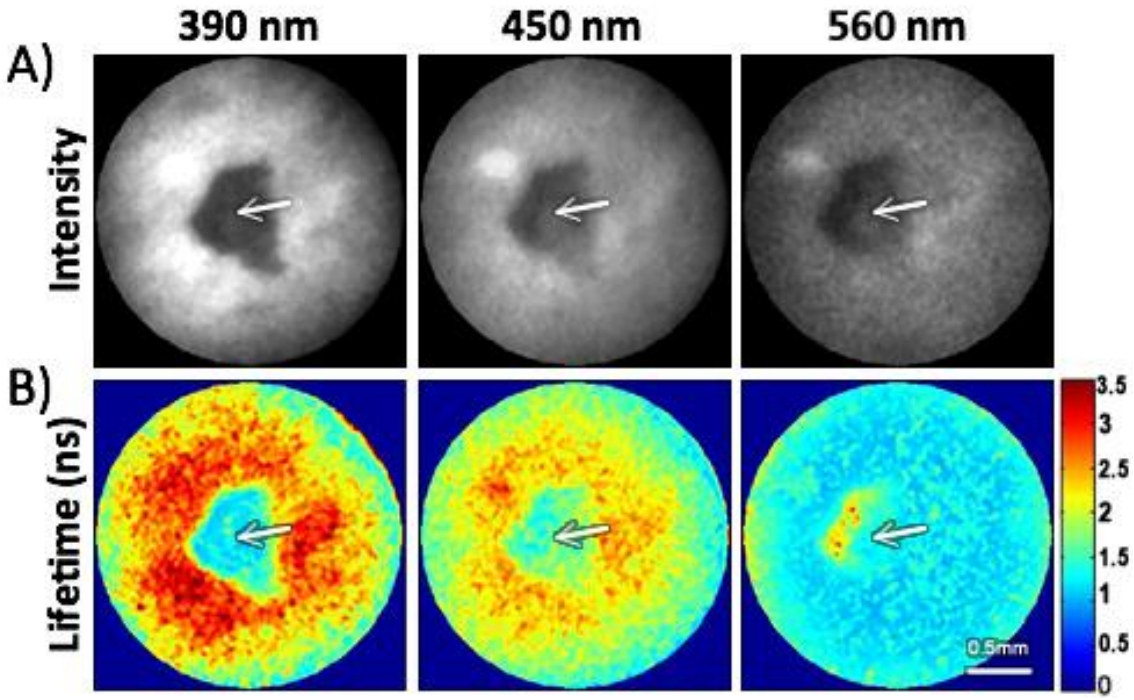

Figure 11: *In vivo* imaging of a DMBA-treated hamster cheek pouch. (A) Fluorescence intensity maps (B) Lifetime maps (colorscale in ns). The arrows indicate a small malignant lesion showing distinct fluorescence intensity and lifetime values than those from the surrounding tissue.

4.4 Discussion

Our *in vitro* and *in vivo* results clearly demonstrate that simultaneous multispectral FLIM imaging can be implemented using the spectral separation scheme proposed in our endoscope design. This flexible FLIM endoscope represents the first design in which both

UV illumination and visible (VIS) fluorescence emission can be transmitted through the same optical path. Although its compact design and fast imaging speed is suitable for clinical application, it suffers from two main disadvantages. First, while the fiber bundle used in this study is the most flexible commercially available bundle with adequate transmission in the UV-VIS range with the added advantage of low UV-induced autofluorescence, its flexibility (minimum bending radius of 200mm) is still far from ideal for many clinical applications. In the future, it is quite possible that more flexible imaging bundles will be custom-fabricated for subsequent designs. For applications where UV illumination is not critical, other more flexible imaging bundles are already commercially available. Second, the fast imaging speed (1 fps) is achieved by utilizing RLD algorithm which only requires two gates for lifetime calculation. The relatively poor temporal resolution of this method may not provide sufficient contrast to detect and differentiate normal, precancer and cancer. To overcome the second disadvantage, we adopted pulse sampling implementation with MCP-PMT instead of ICCD as described in the following chapters.

4.5 Conclusion

We have presented a compact flexible FLIM endoscope system based on a coherent optical fiber bundle suitable for both UV excitation and VIS collection. This system is capable of continuous lifetime imaging for up to three fluorescence emission bands simultaneously. This novel endoscope design was validated by standard fluorescent dyes and a dysplasia lesion from a DMBA-treated hamster cheek pouch. Although it is compact and fast enough for *in vivo* application, the disadvantages discussed in Section 4.4 make

us continue to design another probe based on pulse sampling implementation for the following clinical trial. The new endoscope design will be described in the following chapters.

5. RIGID HANDHELD MULTISPECTRAL FLIM ENDOSCOPE*

5.1 Rigid handheld multispectral FLIM endoscope system

In the previous chapter, we described the design of a fiber bundle based endoscope and discussed its limitations. To overcome these disadvantages, a rigid handheld FLIM endoscope was designed [33]. The system was based on time-domain pulse sampling implementation, similar to the bench-top FLIM system in Chapter 3.

The system consists of a handheld box (volume: 7×13×5 cm^3, mass: 450 g) fitted with a custom-designed rigid endoscope (length: 14 cm, diameter: 1.7 cm) as shown in Fig. 12 (a). The schematic of the proposed system is shown in Fig. 12 (b). A frequency-tripled Q-switched Nd:YAG laser (355 nm, <1 ns pulse width, 100 kHz maximum repetition rate, Advanced Optical Technology) was used as the excitation source. A multimode fiber with core diameter of 25 μm (0.10 NA, HPSC25, Thorlabs) or 50 μm (0.22 NA, FVP050055065, Polymicro Technologies) delivered the excitation light to the handheld box. The excitation light was collimated (L2: f = 11 mm, ARC 350-700 nm, CFC-11X-A, Thorlabs) and scanned by a pair of galvonometer mirrors (5 mm beam aperture, ±5 mechanical degrees, Cambridge Technology) on the proximal end of the rigid endoscope. The rigid endoscope was built using standard ½" lens tubes (Thorlabs) and consisted of three lenses. The first two lenses (L3, L4: f = 30 mm, LB003, Thorlabs) worked as an image relay to extend the length of the endoscope, while the third lens (L4:

* Reprinted with permission from "Handheld multispectral fluorescence lifetime imaging system for *in vivo* applications" by Cheng S., Cuenca R.M., Liu B., Malik B.H., Jabbour J.M., Maitland K.C., Wright J., Cheng Y-S.L., Jo J.A., 2014. Biomedical Optics Express, 5(3), p. 921-931, Copyright [2014] by The Optical Society.

Near UV achromat doublet, f = 30 mm, 50 mm or 60 mm; Edmund Optics) worked as an objective to focus the light on the sample. In this configuration, the excitation fiber core diameter and the focal length of the objective determined the lateral resolution and the FOV of the system. A lens tube with a length equal to the objective's focal length was added at the distal end of the probe which allowed the sample to be in contact with the probe, which can help reduce motion artifact during *in vivo* imaging.

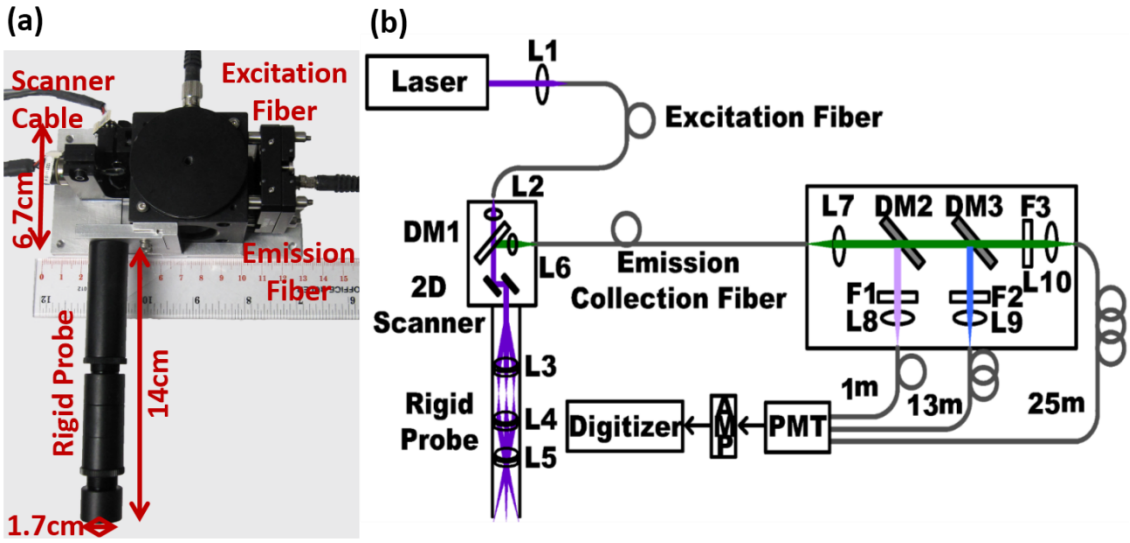

Figure 12: (a) Phtograph of the handheld rigid endoscope (b) Schematic of the rigid FLIM endoscope system. DM: Dichroic mirror, L: Lens, F: Filter, AMP: Amplifier.

An optical simulation of the rigid endoscope design was performed by Zemax (Radiant Zemax) as follows, results of which are presented in Fig. 13. The excitation wavelength for the simulation was set to 355 nm. The setup consisted of a point source (object NA=0.1), a collimator (f=11mm, CFC-11X-A, Thorlabs), a pair of mirror scanners (5 mm in diameter for active area) and the three-lens combination for the endoscope described above. In this configuration, we were able to simulate the FOV by changing the

scan angle of the mirror scanners. By using objective lens with focal lengths of 30mm, 50mm and 60mm, we could vary the FOV. The three colors in Fig. 13 represent light coming from three different scanning angles. The Zemax simulation estimated the numerical aperture of the endoscope at ~0.028 and the maximum FOV of ~5 mm for 30 mm focal length objective, ~10 mm for the 50 mm focal length objective and ~12 mm for the 60 mm focal length objective, which were close to the measured FOV. We also analyzed an intensity line profile across the features of a 1951 USAF resolution target to quantify the lateral resolution [34]. The intensity profile represented the edge-response function and its first-order derivative was the line-spread function (LSF) which was also the cross section of the lateral point spread function (PSF). As an example, for the 25 μm excitation fiber and the 50 mm focal length objective, the FWHM of the PSF was calculated to be 44.8 um, which was in close agreement with the corresponding value experimentally determined by imaging the USAF resolution target as shown in Table 3. Table 3 also provides FOV and lateral resolution values for different combinations of fiber core size and objective's focal length.

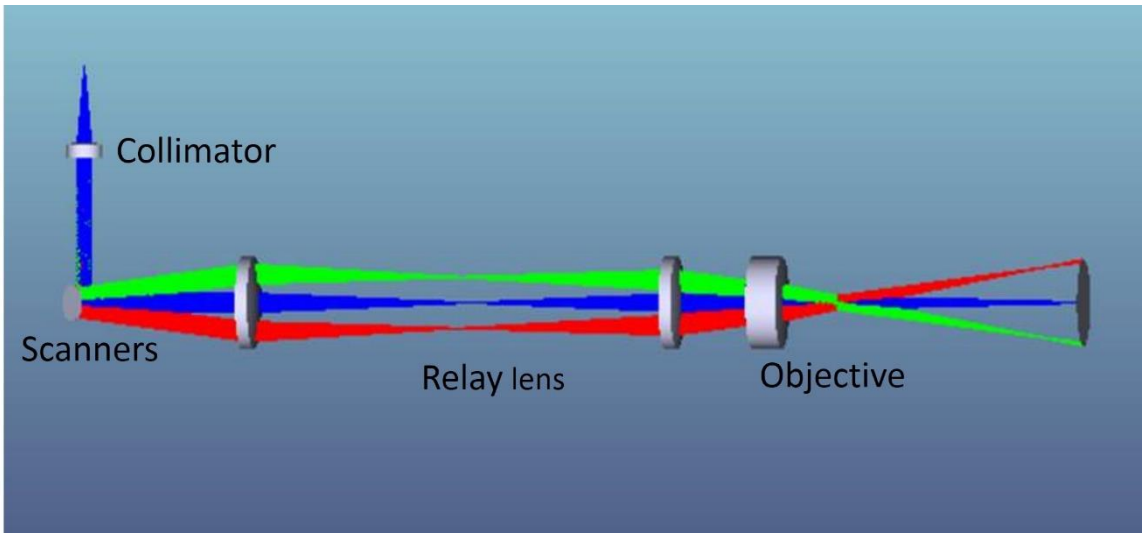

Figure 13: Zemax simulation for the excitation optical pathway. Different colors represent light from different scan angles.

Table 3 Comparison of resolution and FOV with different focal length objectives and excitation fiber core diameters

Excitation fiber core diameter (μm)	Objective focal length (mm)	Lateral resolution (μm)	FOV diameter (mm)
25	f=30	~35	~6.5
	f=50	~50	~11
	f=60	~88	~13
50	f=30	~70	~6.5
	f=50	~110	~11
	f=60	~140	~13

The time-resolved fluorescence emission was spectrally divided in three separate emission bands by the same detection unit as described in Chapter 3. Briefly, as shown in Fig. 12 (b), a set of dichroic mirrors (DM2, DM3) and filters (F1-F3) separated the emission into three spectral bands, each one was coupled into one of the three multimode fiber with different lengths. Thus, for a single excitation pulse, multiple decays corresponding to different spectral bands could be recorded using a single detector. The spectral bands could be customized based on the targeted fluorophores. We selected the

390±20 nm, 452±22.5 nm, and >500 nm bands to optimally distinguish emission from three tissue endogenous fluorophores: collagen, NADH, and FAD, respectively. The multispectral fluorescence signal was detected by a multichannel plate photomultiplier tube (MCP-PMT, 25 ps transient time spread, R3809U-50, Hamamatsu), followed by a preamplifier before being digitized at 6.25 GS/s by a high-speed digitizer (PXIe-5185, National Instruments) resulting in a temporal resolution of 320 ps.

FLIM data obtained from the proposed design was processed using the methods described in Chapter 3. For each sample, nine maps were generated: three absolute intensity maps (I_1, I_2 and I_3), three normalized intensity maps (I_{1n}, I_{2n} and I_{3n}) and three average lifetime maps (τ_1, τ_2 and τ_3). For average lifetime calculation, the relatively broad excitation pulse width (FWHM: ~1 ns) necessitated the temporal deconvolution of the instrument response from the measured fluorescence decay in order to obtain accurate estimation of the fluorescence lifetime. Time deconvolution was performed offline using an optimized Laguerre expansion technique algorithm [24]. The average lifetime τ_{ave} was then estimated from the intrinsic fluorescence decay *h(t)* using the formula $\tau_{ave} = \sum t \cdot h(t) / \sum h(t)$, where *t* is time. Besides the offline lifetime estimation, in order to demonstrate real-time visualization of the multispectral FLIM results, an online deconvolution method was applied, in which the recorded time-resolved decay for each pixel was compared against a lookup table of decays generated by convolving the instrument response with single exponential decays with time constants ranging from 0.2 to 8 ns (in steps of 0.2 ns). The best match in terms of the minimum normalized means squared error provided a single exponential estimation of the fluorescence lifetime.

For all the experiments in this chapter, the following parameters were used. The laser pulse energy at the sample was set at ~1 μJ/pulse, resulting in an adequate signal-to-noise ratio (SNR ≥ 30 dB). Since only one pulse was required per pixel, the pixel rate was equal to the laser repetition rate. The laser repetition rate was set at 30 kHz and the total number of pixels per frame was set at 150×150, corresponding to a frame rate of ~1.33 Hz. The combination of an excitation fiber with a core diameter of 50 μm and an objective with a focal length of 50 mm were adopted, which provided a FOV of ~10mm and a lateral resolution of ~110 μm. This FOV and resolution were suitable for imaging oral cancer.

5.2 Standard dyes validation

The handheld imaging system was first validated with 1 mM solutions of POPOP (in ethanol), NADH and FAD (in PBS). The standard dye solutions were loaded in three quartz capillary tubes and placed side by side under the probe.

The normalized intensity maps (Fig. 14 (a)) confirm strong emission of POPOP at both the 390 nm and 452 nm channels, strongest emission of NADH at the 452 nm channel, and emission of FAD only at the >500 nm channel. The average lifetime maps (Fig. 14 (b)) are also in good agreement with the previously published values for the corresponding fluorophores [24, 32]. The average lifetimes are 1.26 ± 0.05 ns, 0.67 ± 0.06 ns and 2.75 ± 0.03 ns for POPOP, NADH and FAD, respectively.

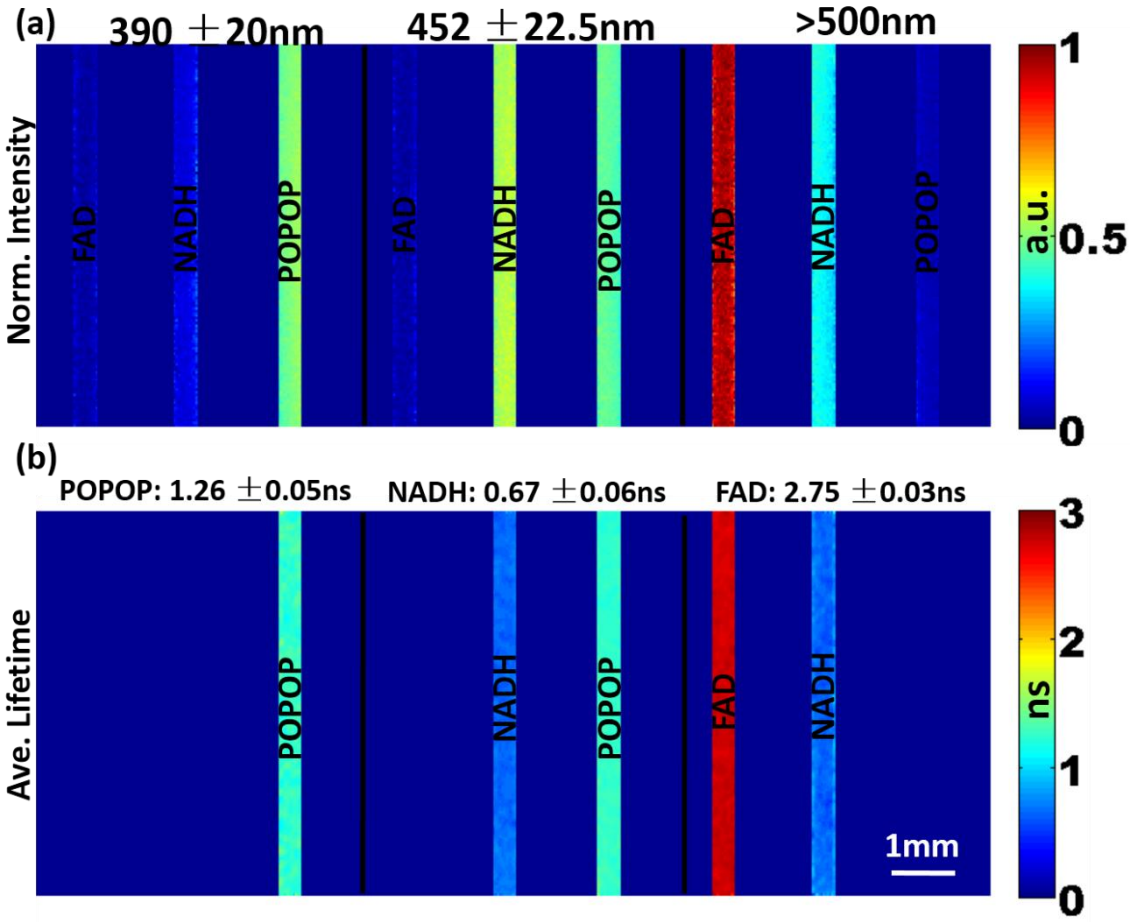

Figure 14: *In vitro* imaging of quartz capillaries loaded with FAD, NADH, and POPOP. (a) Normalized fluorescence intensity maps, and (b) Fluorescence lifetime maps.

In order to demonstrate the system's potential for *in vivo* applications, continuous multispectral imaging was conducted at ~1.33 frames per second. A video, named Media 3 in the supplemental material, was recorded with the online lifetime estimation. The average lifetime values for the dyes using the offline and the online methods are compared in Table 4 (calculated pixel-to-pixel for the areas corresponding to the entire capillary). The offline method provides smaller values than the online method, which is expected because of the assumption for online estimation that the fluorescence decays followed

single exponential decays. But the lifetime value calculated from online method does provide contrast among three fluorescent dyes.

All the videos showed in this chapter were processed with this online method, whereas all the figures in this chapter were processed offline with the Laguerre deconvolution algorithm.

Table 4 Comparison of offline and online fluorescence lifetime estimation (mean ±standard deviation)

	Offline Estimates (ns)	Online Estimates (ns)
POPOP (390 nm)	1.26 ± 0.07	1.03 ± 0.13
NADH (452 nm)	0.67 ± 0.04	0.32 ± 0.08
FAD (>500 nm)	2.75 ± 0.03	1.91 ± 0.14
Pouch (390 nm)	5.86 ± 0.17	3.91 ± 0.58
Pouch (452 nm)	4.44 ± 0.13	2.36 ± 0.45
Pouch (>500 nm)	3.40 ± 0.19	1.92 ± 0.41

5.3 Normal hamster cheek pouch imaging *in vivo*

To demonstrate the ability for *in vivo* application, the handheld system was validated by imaging a normal hamster cheek pouch *in vivo*. The imaging protocol was approved by the IACUC at TAMU. During imaging, the hamster was first anesthetized, a cheek pouch was pulled out and extended, and the rigid probe was gently placed on the mucosa surface.

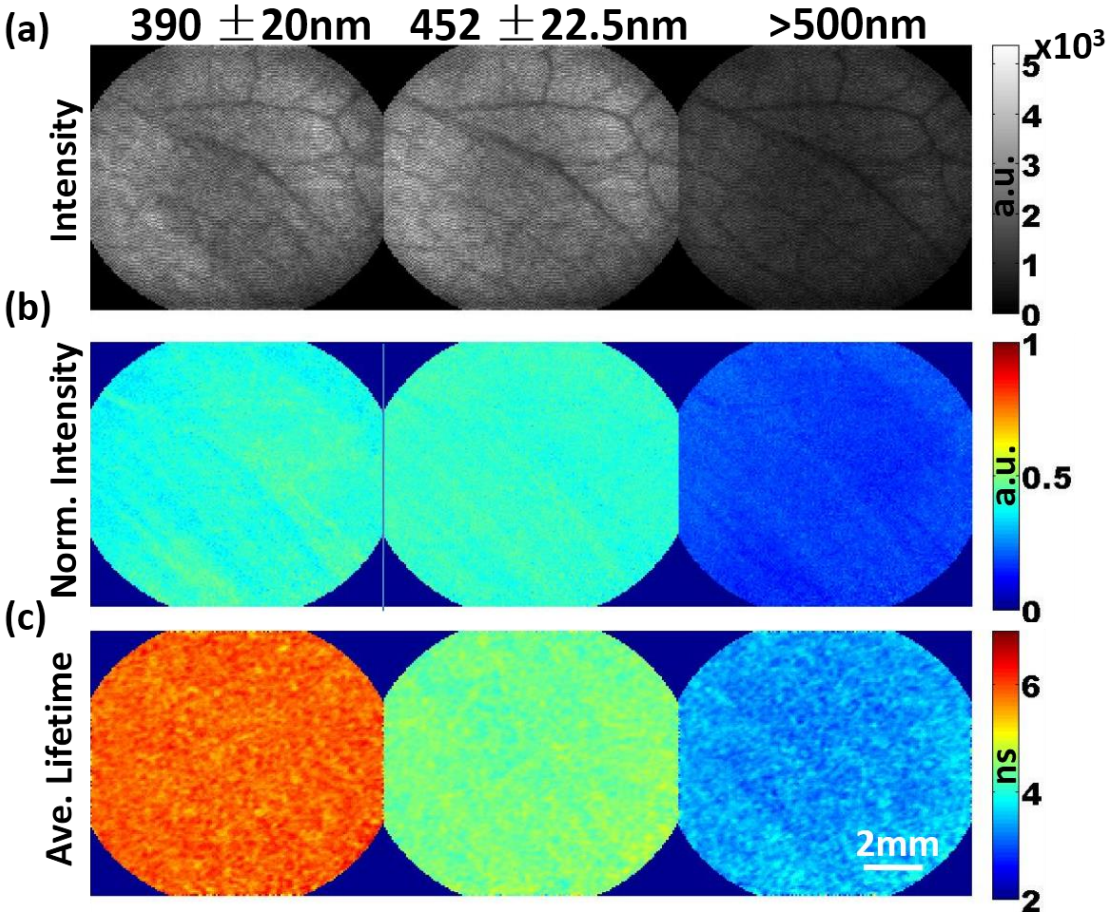

Figure 15: *In vivo* imaging of a normal hamster cheek pouch. (a) Absolute fluorescence intensity maps, (b) Normalized fluorescence intensity maps, and (c) Fluorescence lifetime maps.

Results from an imaged region are shown in Fig. 15. The FLIM maps indicate strong fluorescence intensity at the 390 nm and 452 nm channels (Fig. 15 (a) - (b)), and lifetime values between 4-6 ns (Fig. 15 (c)), reflecting a collagen-dominant autofluorescence expected in normal epithelial tissue. Notice that the vasculature network can be observed in the absolute fluorescence intensity maps, as blood absorption attenuated the fluorescence signal. The normalized intensity and lifetime maps, on the other hand, are

insensitive to blood absorption, and indicate spatially uniform spectral and lifetime properties of the autofluorescence emission of the normal epithelial tissue of a hamster cheek pouch. This is expected, since both the layered structure and the relative concentration of endogenous fluorophores (NADH and FAD in the epithelium, and collagen in the underlying stroma) are maintained throughout the normal epithelial tissue.

A video, named Media 4 in the supplemental material, was recorded during the movement of the probe on top of the mucosa tissue with the real-time online data processing at ~1.33 frames per second. The average lifetimes using either offline or online method are compared in Table 4. In the table, the number are calculated pixel-to-pixel for the area corresponding to the entire FOV. The online method provides smaller values than the offline method, which is expected. But these values does provide a contrast among the different fluorescent components (collagen, NADH and FAD) in epithelial tissue.

5.4 Human oral biopsy imaging *ex vivo*

The clinical potential of this system was further demonstrated by imaging human oral biopsies *ex vivo*. The respective imaging protocols were approved by the Institutional Review Boards (IRB) at TAMU and Baylor College of Dentistry. Tissue samples were obtained from consenting patients who presented themselves either for removal of clinically normal excess tissue or were suspected to have benign, premalignant or malignant lesions. After extraction, the tissue was immediately placed in iced phosphate buffered saline (PBS) solution and transported to the imaging system within 10 minutes. During imaging, the tissue samples were placed in a quartz petri dish. A single FLIM image was recorded with the epithelium in contact with the probe distal end. One part of

the biopsy was sutured to mark the image orientation to allow comparison with the respective histology section. Finally, the tissue specimen was fixed in 10% formalin and processed for hematoxylin and eosin (H&E) histological analysis. The whole procedure was performed within half an hour. Three different types of tissue were imaged, which were classified as normal, benign and premalignant tissue. The results are shown in Fig. 16, Fig. 17 and Fig. 18, respectively.

Fig. 16 shows the FLIM images from a clinically normal oral tissue. For the intensity maps, strong emission are observed at the 452 nm channel, followed by comparatively lower fluorescence at the 390 nm and >500 nm channels. The normalized intensity is 0.27 $\pm$ 0.08, 0.51 $\pm$ 0.05, and 0.23 $\pm$ 0.04 across the normalized intensity maps in Fig. 16 (b) for three spectral channels, respectively. The average lifetime is 4.84 $\pm$ 0.43 ns, 3.95 $\pm$ 0.38 ns and 3.79 $\pm$ 0.28 ns across the lifetime maps in Fig. 16 (c) for the three spectral channels, which indicates collagen is the predominant fluorophore in the sample. Although the absolute fluorescence intensity maps in Fig. 16 (a) show variability across the area of the tissue, the corresponding normalized intensity and lifetime images are relatively uniform. The left border of the tissue has a region where the epithelium layer is absent and underlying connective tissue is exposed. As a result, the normalized intensity and average lifetime in that specific region are increased at the 390nm channel.

Fig. 17 shows FLIM images taken from an oral biopsy of lichen planus, which is a benign inflammatory condition and is usually attributed to a form of autoimmune response. The maps are very similar to those from the normal tissue. The top region is also lack of epithelium layer, which gives variability across the field of view.

Fig. 18 shows FLIM images of an oral biopsy representative of premalignant tissue. The absolute intensity, normalized intensity and average lifetime maps are shown in Fig. 18 (a), 18 (b), and 18 (c), respectively. For the intensity maps, strong emission is observed at the 452 nm channel, followed by comparatively lower fluorescence at the 390 nm and >500 nm channels. For the average lifetime maps, the 452 nm channel show relative shorter lifetime than 390 nm channel attributed to NADH, which show a short lifetime and peak emission at ~450 nm. While most of the FLIM parameters (intensity and lifetime) do not show significant variation across the biopsy, a small region (marked as Region 1 in Fig. 18 (c)) in the lifetime map for >500 nm channel shows a larger value of lifetime (5.19 $\pm$0.30 ns) in contrast to the rest of the biopsy. This area was later diagnosed as superficial invasive squamous cell carcinoma. The corresponding histology image is shown in Fig 18 (d). For comparison, the histology image of a region which representes the rest area of this biopsy (marked as Region 2 in Fig. 18 (c)) with relatively lower lifetime values (4.03 $\pm$ 0.19 ns) is shown in Fig. 18 (e). This particular region in Fig. 18 (e) was diagnosed as dysplasia as most of the biopsy. The increased lifetime in Region 1 can be attributed to poryphirin, the presence of which is known to increase with the progression of precancer and has a relatively long lifetime (>6 ns) [18].

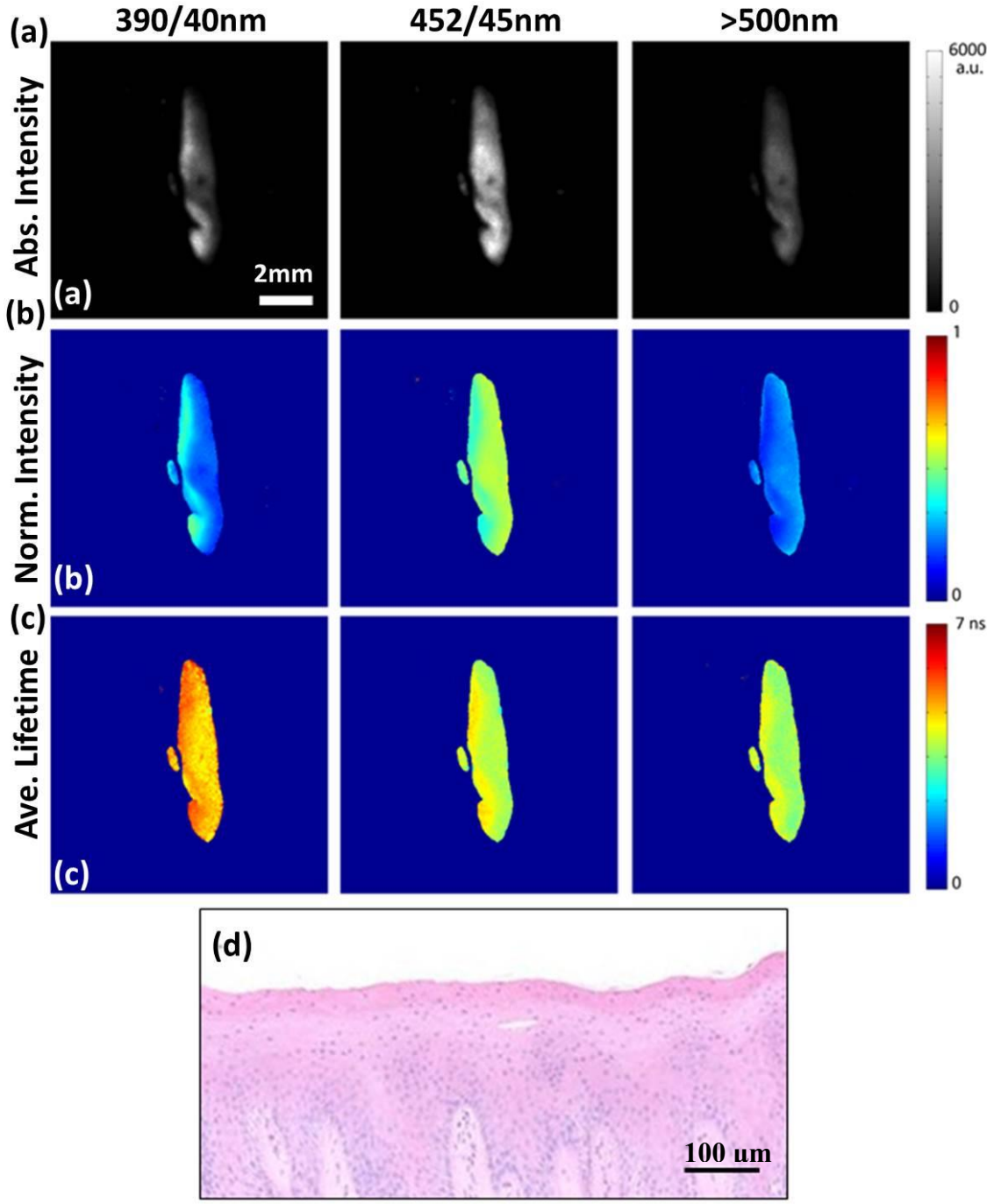

Figure 16: FLIM images of clinically normal tissue from gingiva. (a) Absolute fluorescence intensity (b) Normalized fluorescence intensity, and (c) Average lifetime maps for 390nm, 450nm and >500nm spectral channel, respectively. (d) Image of the corresponding histology section.

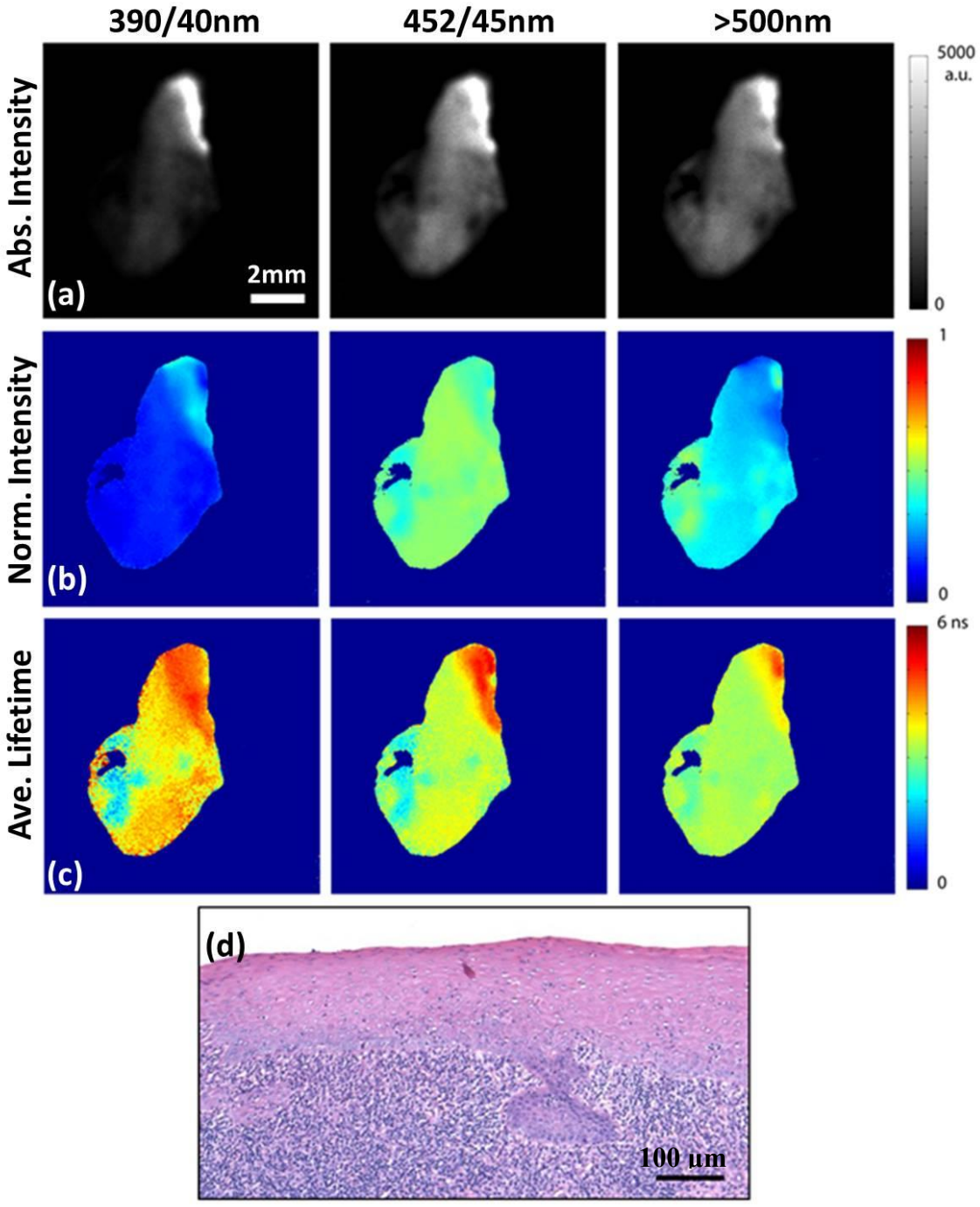

Figure 17: FLIM images of the benign lesion classified as oral lichen planus. (a) Absolute fluorescence intensity (b) Normalized fluorescence intensity, and (c) Average lifetime maps for 390nm, 450nm and >500nm spectral channel, respectively. (d) Image of the corresponding histology section.

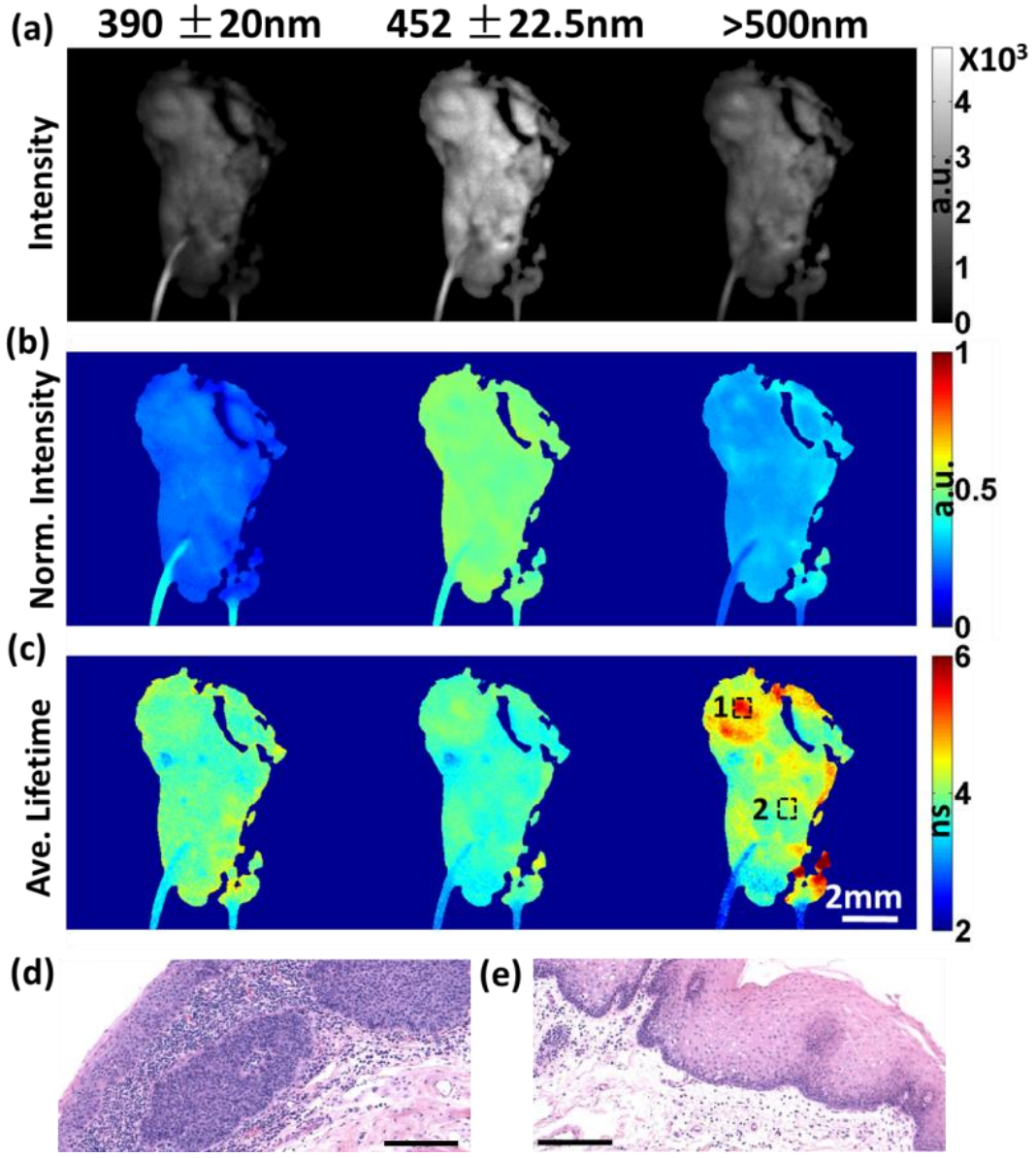

Figure 18: FLIM images of the premalignant tissue. (a) Absolute integrated fluorescence intensity maps, (b) Normalized integrated fluorescence intensity maps, and (c) Aerage lifetime maps. The thread at the bottom of (a), (b) and (c) is the suture used to mark the tissue orientation for histology study. (d) Histology image for the position marked in (c) as Region 1 which was diagnosed as superficial invasive squamous cell carcinoma. (e) Histology image for the position marked in (c) as Region 2 which was diagnosed as dysplasia. Both Region 1 and Region 2 are squares of 600×600 μm^2. The scale bars in both (d) and (e) represent 200μm.

5.5 Normal human oral mucosa imaging *in vivo*

The system was further validated by imaging human oral mucosa from normal volunteers. The imaging protocols were approved by the Institutional Review Boards (IRB) at TAMU and Baylor College of Dentistry. The ventral surface of a normal human tongue was imaged *in vivo*. The probe was inserted into the volunteer's month and gently placed on the target location. Only one frame was collected to minimize exposure to UV radiation.

The absolute intensity, normalized intensity and average lifetime maps are shown in Fig. 19. Strong emission is observed in 452 nm channel, followed by comparatively lower fluorescence at 390 and >500 nm channels. The average lifetime maps show similar lifetime of 4.04 ± 0.29 ns, 4.22 ± 0.28 ns and 4.19 ± 0.28 ns for 390 nm, 452 nm and >500 nm channels, respectively. Notice also here that spatial contrast is evident in the absolute fluorescence intensity maps, while little contrast is observed in the normalized intensity and lifetime maps, as expected for normal epithelial tissue.

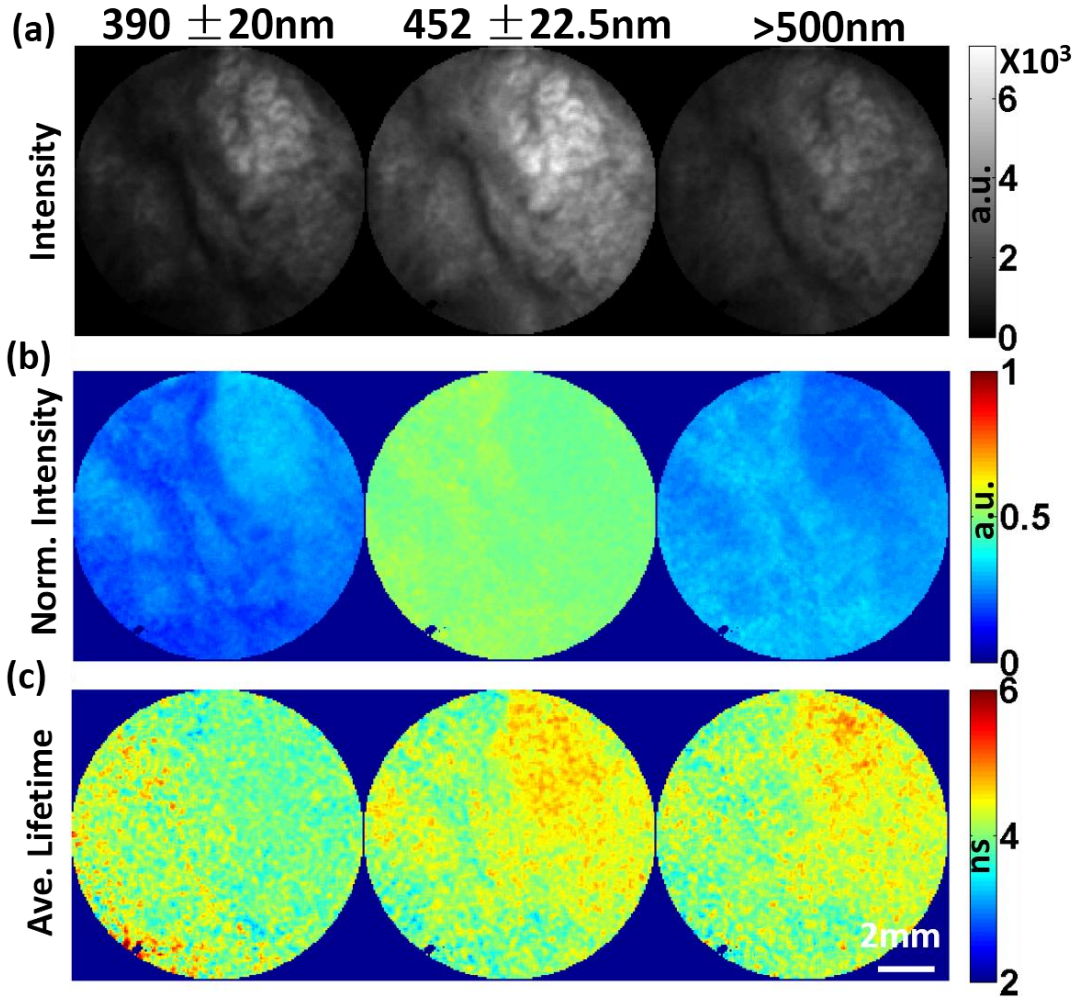

Figure 19: *In vivo* imaging of the ventral tongue from a normal human volunteer. (a) Absolute integrated fluorescence intensity maps, (b) Normalized integrated fluorescence intensity maps, and (c) Fluorescence lifetime maps.

5.6 Clinical validation in human subjects *in vivo*

Patients with suspected lesion were included for this study. The diseased human oral mucosa was imaging *in vivo*. The imaging protocols were approved by the Institutional Review Boards (IRB) at TAMU and Baylor College of Dentistry. Only one frame was collected to minimize exposure to UV radiation. The laser power deposited on tissue

surface was calculated to be below the maximum permissible exposure (MPE) of the tissue damage threshold by referring the American National Standards Institute (ANSI) standards for the safe use of lasers on skin. The detailed calculation can be found in Section 5.7. In order to facilitate this imaging process, the system was moved to bedside in the clinic. The patients were first inspected by physicians and the ones who were referred for a biopsy or oral surgery were asked whether they were willing to join our study. The consented patient was imaged *in vivo* by the physician on the lesion. After the *in vivo* imaging, the patient would be sent for either biopsy collection or oral surgery to remove part or the whole lesion where we did the *in vivo* imaging. The incised tissue was imaged *ex vivo* under our system as comparison and sent for H&E histological analysis.

Fig. 20 and Fig. 21 show the results of the *in vivo* and *ex vivo* imaging for the same lesion of a patient. The absolute intensity, normalized intensity and average lifetime maps for *in vivo* imaging are shown in Fig. 20 (a), 20 (b), and 20 (c), respectively. For the intensity maps, strong emission is observed at the 452 nm channel, followed by comparatively lower fluorescence at the 390 nm and >500 nm channels. For the average lifetime maps, a change of lifetime is shown across the FOV in the 390 nm channel in Fig. 20 (c). The left part which is normal tissue shows longer lifetime than the right part which was diagnosed as dysplasia by histologist. White arrows indicate the margin between the normal tissue and dysplasia tissue. The longer lifetime value suggests that the dominant fluorophore is collagen, and the shorter lifetime of dysplasia tissue can be attributed to the increase of NADH. These results are consistent with the biochemical composition of

normal and dysplasia tissue. The average lifetime for the right part in 390 nm channel is 4.02 ± 0.28 ns in contrast to 2.70 ± 0.27 ns for the left part.

For comparison, the biopsy taken from the same lesion was imaged *ex vivo*. The absolute intensity, normalized intensity and average lifetime maps for *ex vivo* imaging are shown in Fig. 21 (a), 21 (b), and 21 (c), respectively. For the intensity maps, strong emission is observed at the 452 nm channel, followed by comparatively lower fluorescence at the 390 nm and >500 nm channels. For the average lifetime maps, a change of lifetime is shown in the 390 nm channel in Fig. 21 (c), in which the center part shows a shorter lifetime than the rest of the tissue. This specific region with shorter lifetime corresponds to the left part of the tissue in Fig. 20 (c), was histopathologically diagnosis as dysplasia (histology image shown in Fig. 21 (d)). White arrows indicate the same margin between the normal tissue and dysplasia tissue as in Fig. 20 (c). The shorter average lifetime in 390 nm channel is 3.08 ± 0.26 ns in contrast to 4.62 ± 0.26 ns of the longer average lifetime, which are in agreement with the results from the *in vivo* imaging. In addition, the absolute intensity maps of Fig. 20 (a) and Fig. 21 (a) also show similar structure for *in vivo* imaging and *ex vivo* imaging, which is also an indicator to correlate *in vivo* imaging and *ex vivo* imaging.

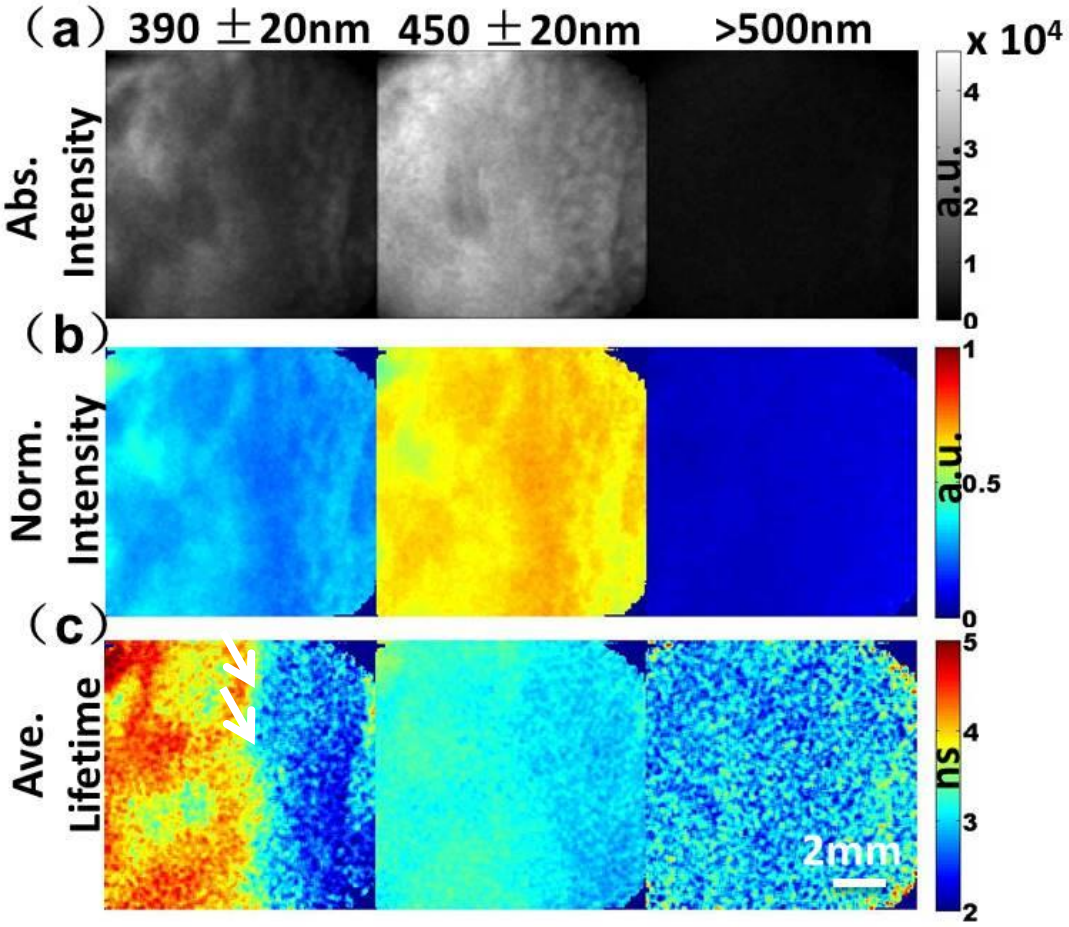

Figure 20: *In vivo* imaging of the dysplasia tissue. (a) Absolute integrated fluorescence intensity maps, (b) Normalized integrated fluorescence intensity maps, and (c) Average lifetime maps. White arrows show the margin between the normal and dysplasia tissue.

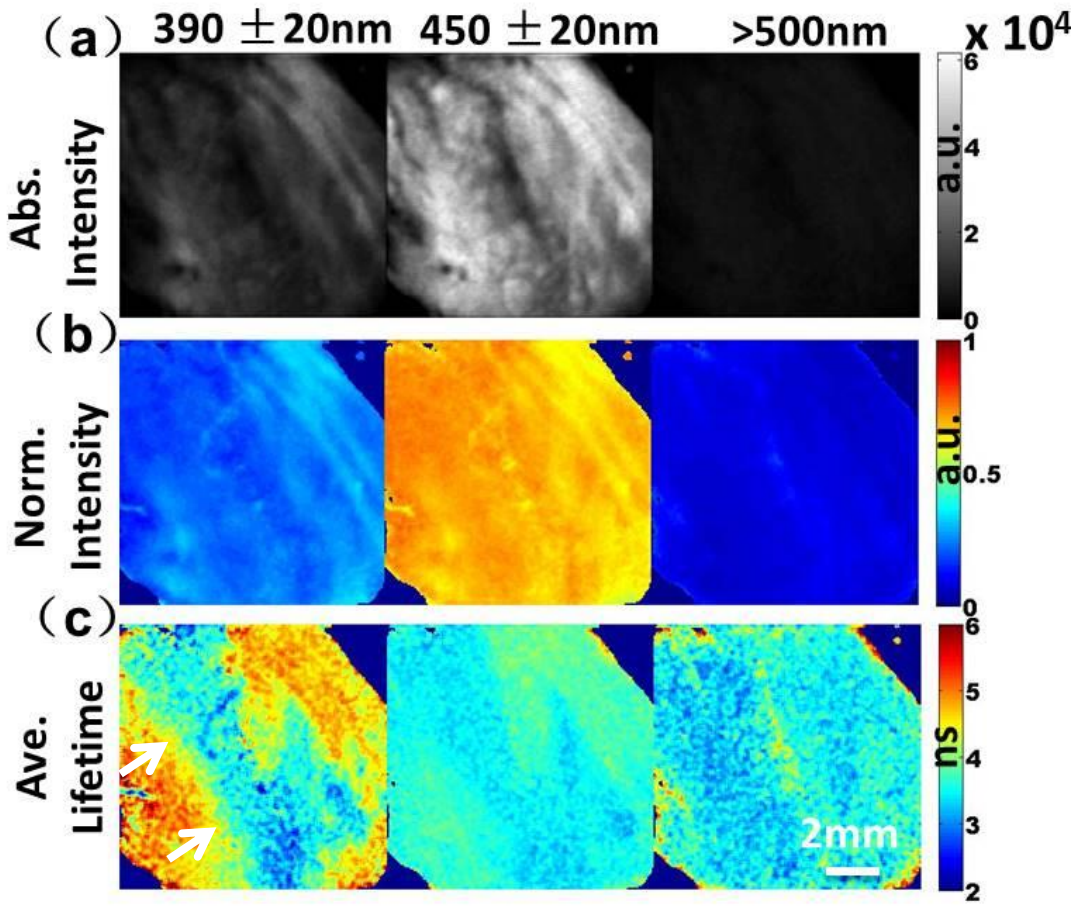

Figure 21: *Ex vivo* imaging of oral biopsy taken from the same lesion in Fig. 20. (a) Absolute integrated fluorescence intensity maps, (b) Normalized integrated fluorescence intensity maps, and (c) Average lifetime maps. White arrows show the margin between the normal and dysplasia tissue.

5.7 Discussion

As stated before, a pulse energy of 1 μJ at the sample provides an adequate SNR per pixel; thus, the pixel rate equates to the laser repetition rate. Since the frame rate is determined by the pixel rate and the number of pixels per frame, imaging speed can be increased by either increasing the laser repetition rate or decreasing the number of pixels

per frame. The number of pixels per frame can be reduced without sacrificing lateral resolution if the FOV is also reduced accordingly; thus, higher frame rates can be achieved at smaller FOV. Increasing the laser repetition rate while maintaining the pulse energy will increase the average power transmitted through the excitation fiber and ultimately deposited on the sample. Thus, the maximum average power that can be practically applied is ultimately limited by the damage threshold of both the excitation fiber and the sample. For all the experiments, the laser repetition rate was limited to 30 kHz in order to avoid rendering permanent damage to the input facet of the excitation fiber (observed at higher repetition rates). To increase the frame rate, the use of other excitation fibers capable of handling higher average power levels (thus higher pixel rate) is currently being explored.

The tissue damage threshold can be estimated in terms of the maximum permissible exposure (MPE) provided by the American National Standards Institute (ANSI) standards for the safe use of lasers on skin [35]. Since the excitation we use is a repetitive-pulse laser. There are two rules to follow: the exposure of the skin shall not exceed the MPE based upon a single-pulse exposure, and the average irradiance of the pulse train shall not exceed the MPE applicable for the total pulse train. In our case, the single-pulse limit for a 1 ns pulse exceeds 300 μJ in the limiting aperture (φ = 3.5 mm) which is much higher than the energy we use. As a result, we will be limited by the total energy deposited over the dwell time. According to the standard, there are thermal and photochemical effects, between which the smaller MPE value should be follow. According to the standard, the

thermal MPE yields smaller value. The equation to calculate the thermal MPE is in Eq. 5.1

$$MPE = 0.56\, t^{0.25}\ (J/cm^2) \tag{5.1}$$

It is defined in a limiting aperture φ = 3.5 mm. The equation should be modified as in Eq. 5.2 if the aperture are is considered.

$$MPE = 0.56\ \times \pi\, r^2 t^{0.25} = 0.56 \times (3.14) \times (0.175)^2 \times t^{0.25}\ (J) \tag{5.2}$$

The dwell time *t* in Eq. 5.1 and Eq. 5.2 is equal to *s/f*, where *s* is the total number of pulses applied inside the limiting aperture, and *f* is the laser repetition rate. Since only one pulse is applied per pixel, *s* equates to the total number of pixels inside the limiting aperture. In our *in vivo* experiments, the laser repetition rate was 30 kHz with a pulse energy of ~1 μJ, and the number of pixels per frame was set at 150 × 150 for a FOV of 10 × 10 mm^2. Thus, based on the Eq. 5.2, the MPE is E (J) = 5.39 × 10^{-2} × (s/f) $^{0.25}$ = 5.39 × 10^{-2} × (2164 / 30,000) $^{0.25}$ = 27.9 mJ. The actual energy deposited is E (J) = 53 × 53 × 10^{-3} mJ = 2.2 mJ, which is an order of magnitude lower than the MPE. We are thus confident that *in vivo* imaging can be performed safely with the proposed handheld FLIM imaging system.

One significant advantage of the proposed multispectral FLIM probe design is that, unlike previous implementations [8-10, 27], it can achieve relatively high imaging speed without sacrificing temporal resolution. The achieved high temporal resolution allows correcting for the non-ideal instrument response through time deconvolution. In addition, since the entire fluorescence decay is directly measured, the full complexity of its temporal dynamics can be captured and is no longer limited to a single exponential approximation.

Although our imaging systems allows measuring time-resolved fluorescence data with high temporal resolution, accurate estimation of fluorescence lifetimes still requires computationally expensive iterative deconvolution methods. Our fully validated Laguerre deconvolution method is significantly faster than standard nonlinear least square deconvolution algorithms, but it is still not suitable for online processing and visualization of FLIM data [24]. To take advantage of the relative high pixel rate achieved by our system and to demonstrate real-time FLIM data processing and visualization (as shown in Media 3 and Media 4 in the supplemental material), the online deconvolution method described above was proposed. An interesting observation was the fact that the online processing and visualization of the multispectral FLIM maps were insensitive to movement (as shown in the videos). In Table 4, the values of the online lifetime estimations are compared against the offline estimations obtained with the Laguerre deconvolution method. As expected, the online values were underestimated with respect to the offline values due to the single exponential approximation. Nevertheless, the online FLIM maps provided fluorescence lifetime contrast similar to that of the offline FLIM maps.

While the >500 nm emission band was provided to target and isolate fluorescence from FAD, there can be a significant contribution of fluorescence from poryphrin in precancerous and cancerous areas, and can potentially confound the signal in that band. The presence of poryphrin is usually attributed to changes associated with malignant transformation, and wherein the level of poryphrin is usually elevated in the effected tissue [36]. In our study, the effect of poryphrin manifested in Fig. 18 where the fluorescence lifetime in the region with invasive carcinoma showed a relative increase due to longer

lifetime of poryphrin [36]. For the future, we will consider adding another emission window corresponding to poryphrin (peak emission: ~630 nm). In addition to isolating fluorescence from FAD, adding of fourth spectral window can offer us another parameter to characterize the progression of precancer.

As mentioned above, our target application was to image the oral mucosa *in vivo*. Our clinical collaborators (Dr. Lisa Cheng and Dr. John Wright) have indicated that the length of our current endoscope (14 cm) is appropriate to image the oral cavity, as we have successfully imaged a lot of patients *in vivo*. Nevertheless, the doctors indicated an endoscope design with even smaller size and less weight would be more convenient for handling and easily to access some specific narrow location inside the oral cavity according to their experience to operate the current system.

5.8 Conclusion

In summary, we reported the first demonstration of a time-domain multispectral FLIM endoscope that required only one excitation pulse per pixel; thus, the pixel rate was equal to the laser repetition rate. Taking advantage of this relatively high pixel rate, we were able to perform the fastest *in vivo* multispectral FLIM imaging in the human oral cavity reported thus far. Finally, we also reported the first demonstration of real-time deconvolution of the instrument response from the fluorescence decay at each pixel of the image, which allowed real-time lifetime map estimation and visualization at multiple spectral bands simultaneously. This design will facilitate the evaluation of multispectral FLIM for detecting oral cancer and precancer.

6. CLINICAL PROTOTYPE OF RIGID HANDHELD FLIM ENDOSCOPE

6.1 Clinical prototype of rigid handheld FLIM endoscope

As described in Section 5.7, reducing the size and the weight of the handheld system can potentially aid in probing most of the oral cavity *in vivo*. To this end, we constructed a relatively smaller version of the rigid handheld FLIM system with MEMS scanning mirrors and lenses with smaller diameters (6.25mm in diameter). This system will be served as the clinical prototype for in vivo study in the future. A photograph of the handheld part of the new system is shown in Fig. 22 (a). It was approximately 250 gram in weight with a handheld package of $10 \times 5 \times 3$ cm^3 in volume. A rigid probe (length: 11cm, diameter: 0.8cm) was fitted onto the handheld package. The system schematic is shown in Fig. 22 (b). Pulsed UV excitation light from a frequency-tripled Q-switched Nd:YAG laser (355 nm, <1 ns pulse width, 100 kHz maximum repetition rate, Advanced Optical Technology) was delivered to the system through a multimode fiber (50 μm core diameter, FG050LGA, Thorlabs), and collimated by an aspherical lens (f = 8mm, A240TM-A, Thorlabs). The collimated excitation was reflected by a dichroic mirror (1/2 inch diameter, 377drz, Chroma) which was used to separate the UV excitation and visible fluorescence emission, and deflected by a two dimensional MEMS scanning mirror (4.2mm active area, -5° to +5° mechanical angle, Mirrorcle) onto the rigid probe. The dichroic mirror and MEMS scanning mirror were mounted at a 45° angle to the incoming excitation light in a custom-machined housing. A three-adjuster kinematic mirror mount (KCB05, Thorlabs) was integrated in the housing to mount the dichoric mirror. It allowed slight angle adjustment in order to compensate for any inaccuracies introduced during

machining of the housing. The housing was made from aluminum. The rigid probe was custom-designed with four achromat lenses (f = 30 mm, 6.25 mm diameter, Edmund Optics). Two of these lenses formed an image relay to extend the length of the probe as described in the previous handheld system. Another lens at the distal end worked as an objective to focus the light onto the sample. A fourth lens was placed in the intermediate image plane of the relay lens pair to serve as a field lens which increased the FOV from ~3.6 mm to ~5 mm. Fig. 23 shows the Zemax simulation for the rigid probe both with and without the field lens. The three colors in Fig. 23 represent three different scanning angles. As seen in the three-lens system, the marginal light is out of the range of the second lens of the relay lens pair. After adding the field lens between the relay lens pair, the clipping of beam at the edge is eliminated. As a result, the scan angle is enlarged after adding the field lens.

To assemble the probe, the four lenses were fixed with UV cured glue (NOV 63, Edmund Optics) inside a tube (Inner diameter = 6.35 mm, outer diameter = 7.14mm, McMaster Carr). The distance between the lenses should be decided by Zemax simulation and free-space test in order to optimize the optical performance of the probe. Small slits were made in specific positions on the tube to apply the UV glue. An outer tube (inner diameter = 7.41mm, outer diameter = 7.93mm, McMaster Carr) was used to seal the probe.

The fluorescence emission was collected by the same rigid probe, de-scanned by the MEMS mirror and passed the dichroic mirror (DM1 in Fig. 22(b)) to the multispectral detection unit which was the same as described in Section 3.1 and Section 5.1. The time-resolved fluorescence emission was spectrally divided in three separate emission bands:

390±20 nm, 452±22.5 nm, and >500 nm bands corresponding to peak emission wavelength of endogenous fluorophores of collagen, NADH and FAD, respectively. The multispectral fluorescence signal was detected by a multichannel plate photomultiplier tube (MCP-PMT, 25 ps transient time spread, R3809U-50, Hamamatsu), followed by a preamplifier before being digitized at 6.25 GS/s by a high-speed digitizer (PXIe-5185, National Instruments) resulting in a temporal resolution of 320 ps.

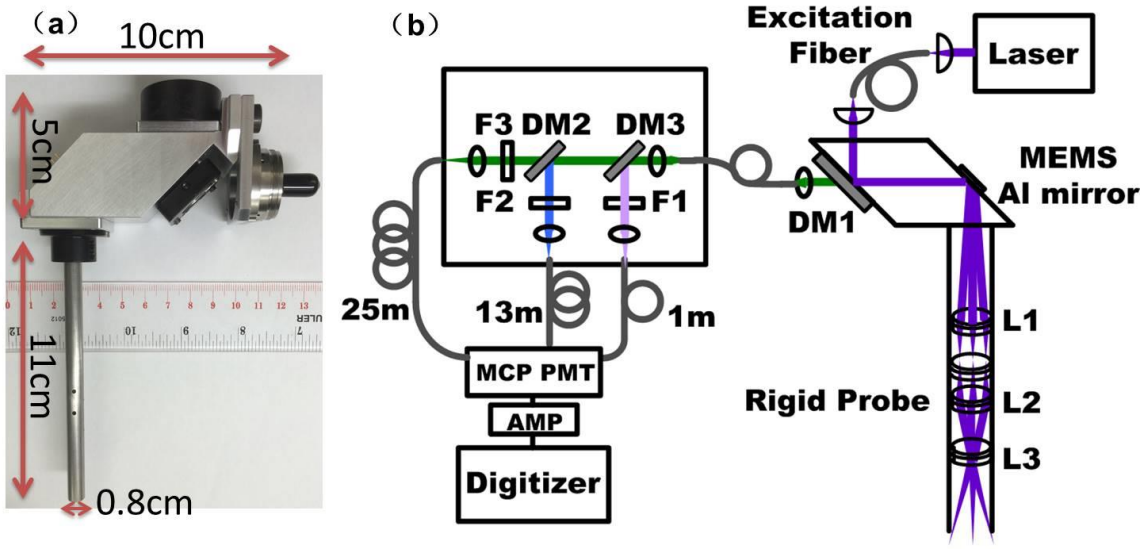

Figure 22: (a) Photograph of the clinical prototype of the handheld probe (b) Schematic of the clinical prototype of the FLIM endoscope system. DM: Dichroic mirror, L: Lens, F: Filter, AMP: Amplifier.

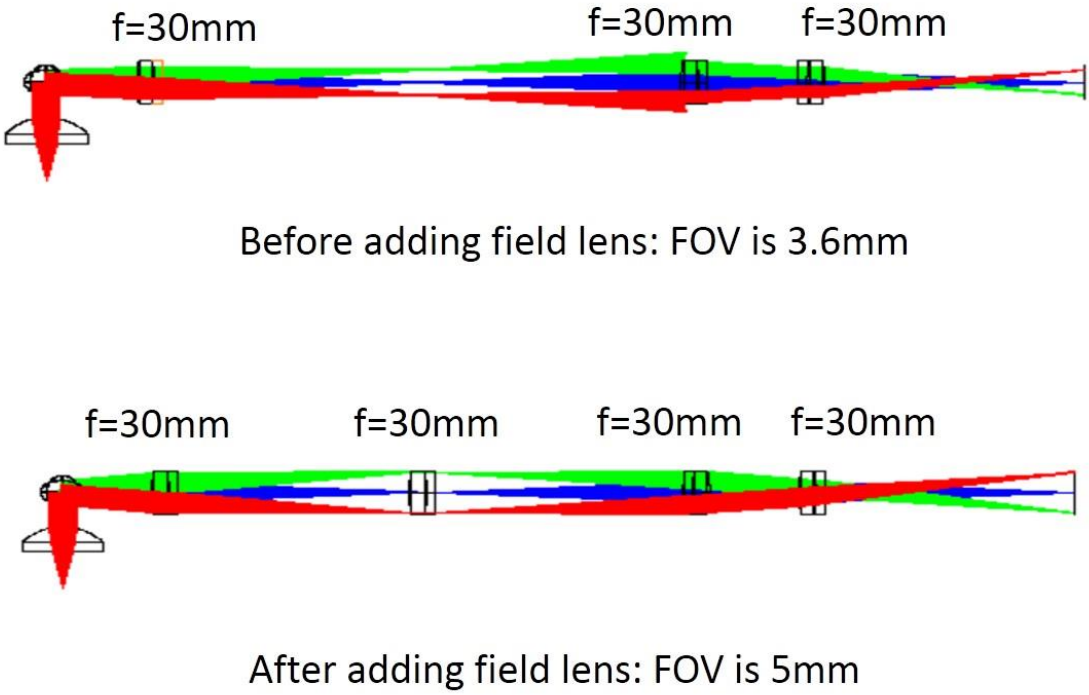

Figure 23: Zemax simulation of the FOV (top) before adding the field lens and (bottom) after adding the field lens.

Data processing was similar to that described in Chapter 3 and Chapter 5. For each sample, nine maps were generated: three absolute intensity maps (I_1, I_2 and I_3), three normalized intensity maps (I_{1n}, I_{2n} and I_{3n}) and three average lifetime maps (τ_1, τ_2 and τ_3). For average lifetime calculation, the relatively long excitation pulse width (FWHM: ~1 ns) necessitated the temporal deconvolution of the instrument response from the measured fluorescence decay in order to obtain accurate estimation of the fluorescence lifetime. Time deconvolution was performed offline using an optimized Laguerre expansion technique algorithm [24]. The average lifetime τ_{ave} was then estimated from the intrinsic fluorescence decay $h(t)$ with $\tau_{ave} = \sum t \cdot h(t) / \sum h(t)$, where t was time. Besides the offline

lifetime estimation, in order to demonstrate real-time visualization of the multispectral FLIM maps, an online deconvolution method was applied, in which the recorded time-resolved decay for each pixel was compared against a lookup table of decays generated by convolving the instrument response with single exponential decays with time constants ranging from 0.2 to 8 ns (in steps of 0.2 ns). The best match in terms of the minimum normalized means squared error provided a single exponential estimation of the fluorescence lifetime.

For all the experiments in this chapter, the following working parameters were used. The laser pulse energy at the sample was set at ~1 μJ/pulse, resulting in an adequate signal-to-noise ratio (SNR ≥ 30 dB). Since only one pulse was required per pixel, the pixel rate was equal to the laser repetition rate. The laser repetition rate was set at 10 kHz and the total number of pixels per frame was set at 160×160, corresponding to an acquisition speed of ~0.4 Hz. The lateral resolution was measured to be ~100 μm by USAF target (#53715, Edmund Optics).

6.2 Standard dyes validation

The new handheld imaging system was first validated with 1 mM solutions of POPOP (in ethanol), NADH and FAD (in PBS). The standard dye solutions were loaded in three quartz capillary tubes and placed side by side under the probe.

The normalized intensity maps (Fig. 24 (a)) confirm strong emission of POPOP at both the 390 nm and 452 nm channels, strongest emission of NADH at the 452 nm channel, and emission of FAD only at the >500 nm channel. The average lifetime maps (Fig. 24 (b)) are also in good agreement with the previously published values for the

corresponding fluorophores [24, 27, 33]. The average lifetime for POPOP is 1.23±0.03 ns for 390 nm channel and 1.12±0.02 ns for 452 nm channel. The average lifetime for NADH is 0.30±0.05 ns for 452 nm channel and 0.21±0.09 ns for >500 nm. The average lifetime for FAD is 2.14±0.05 ns for >500 nm channel.

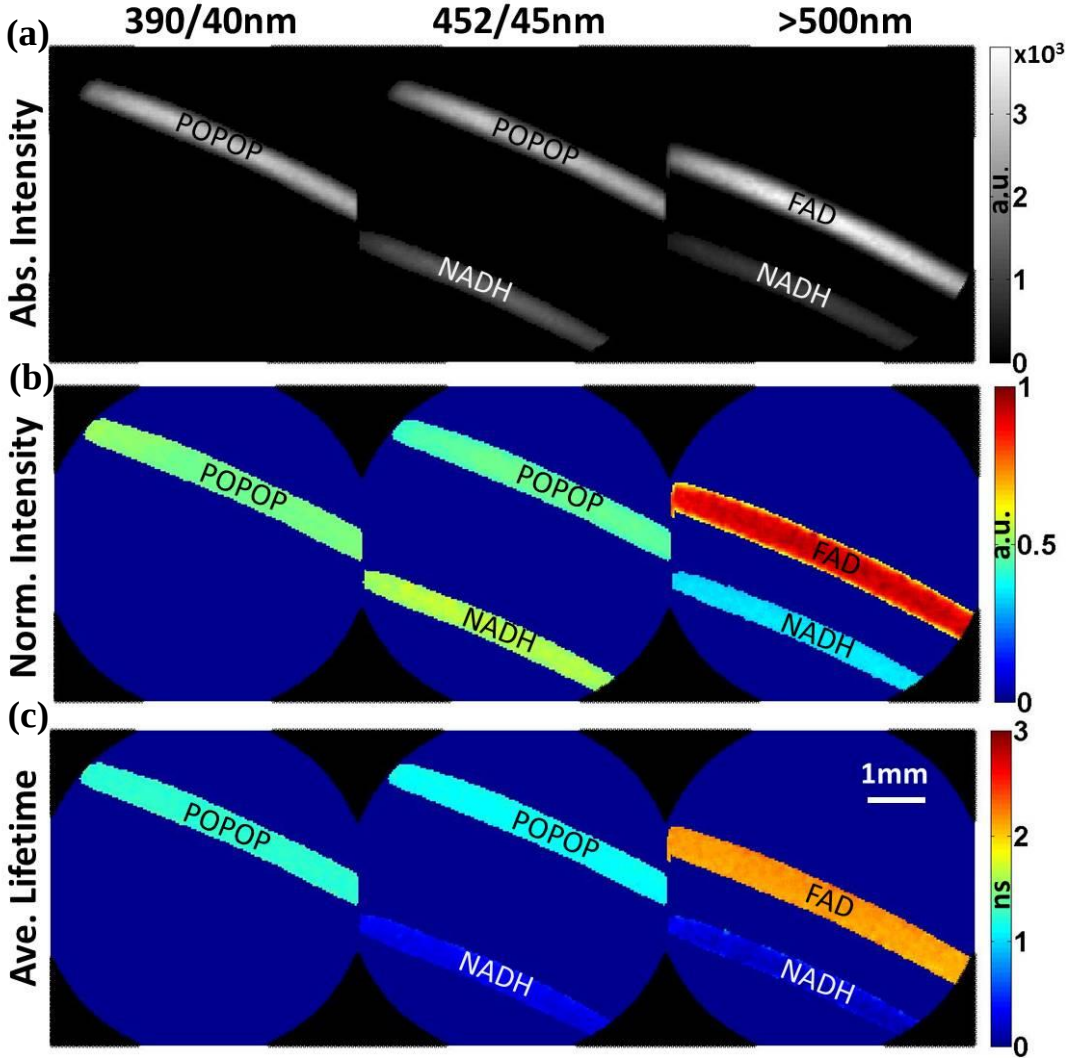

Figure 24: *In vitro* imaging of quartz capillaries loaded with FAD, NADH, and POPOP. (a) Normalized fluorescence intensity maps, and (b) Fluorescence lifetime maps.

6.3 Normal human oral mucosa imaging *in vivo*

The system was validated by imaging human oral mucosa *in vivo* from normal volunteers. The imaging protocols were approved by the Institutional Review Boards (IRB) at TAMU and Baylor College of Dentistry. The ventral surface of a normal human tongue was imaged *in vivo*. The probe was inserted into the volunteer's month and gently placed on the target location. Only one frame was collected to minimize exposure to UV radiation.

The absolute intensity, normalized intensity and average lifetime maps are shown in Fig. 25. Strong emission is observed in 452 nm channel, followed by comparatively lower fluorescence at 390 and >500 nm channels. The average lifetime maps show similar lifetime of 4.12 ± 0.20 ns, 4.12 ± 0.24 ns and 3.66 ± 0.17 ns for 390 nm, 452 nm and >500 nm channels, respectively. Notice also here that spatial contrast is evident in the absolute fluorescence intensity maps, while little contrast is observed in the normalized intensity and lifetime maps, as expected for normal epithelial tissue.

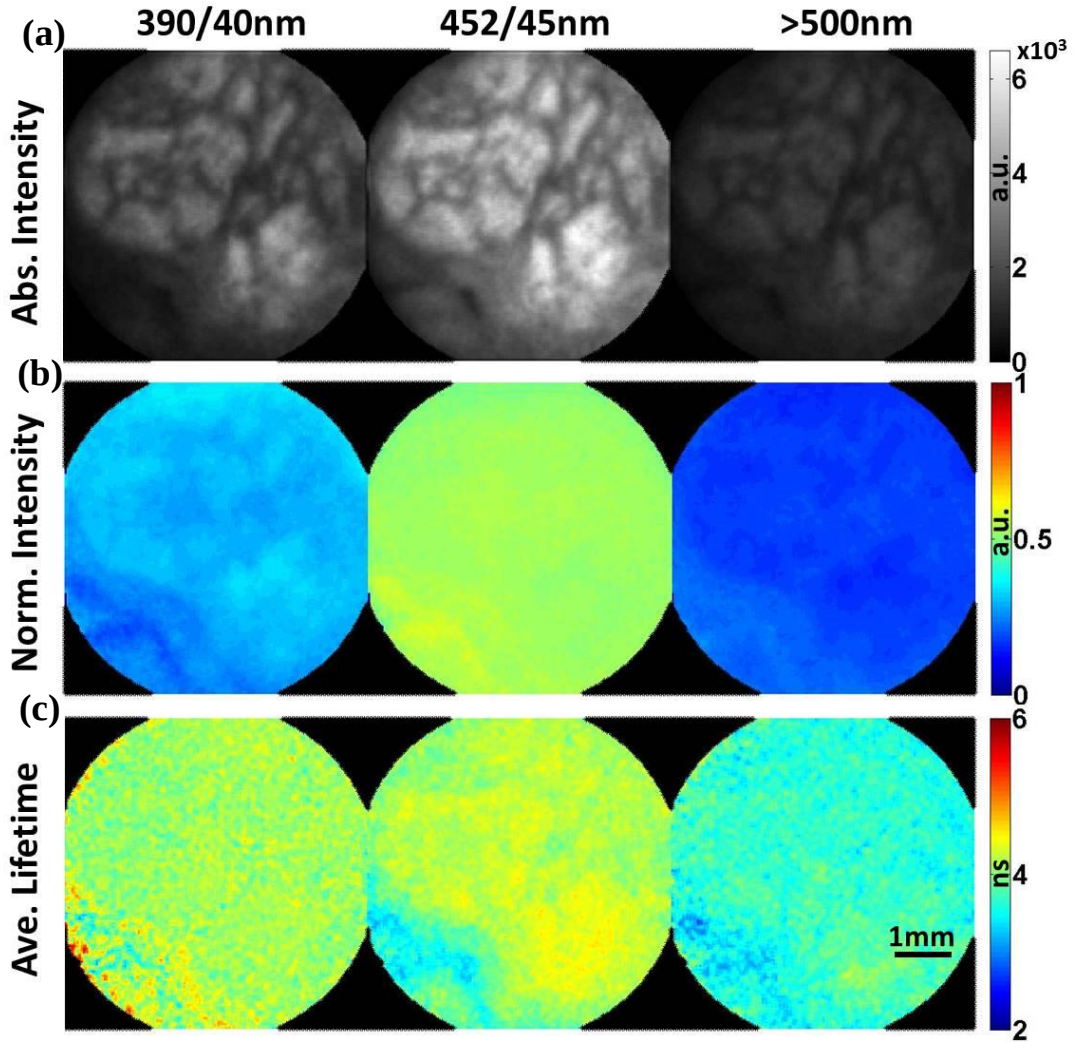

Figure 25: *In vivo* imaging of the ventral tongue from a normal human volunteer. (a) Absolute integrated fluorescence intensity maps, (b) Normalized integrated fluorescence intensity maps, and (c) Fluorescence lifetime maps.

6.4 Oral biopsy imaging *ex vivo*

Fig. 26 shows FLIM images of a tissue biopsy. The absolute intensity, normalized intensity and average lifetime maps are shown in Fig. 26 (a), Fig. 26 (b), and Fig. 26 (c), respectively. For the intensity maps, strong emission is observed at the 452 nm channel, followed by comparatively lower fluorescence at the 390 nm and >500 nm channels. For

the average lifetime maps, the 452 nm channel shows relative shorter lifetime than the 390 nm channel attributed to NADH, which shows a short lifetime and peak emission at ~450 nm. This indicates collagen is the predominant fluorophore in the sample which is similar to that in normal tissue or a benign lesion. At first, this lesion was clinically diagnosed as dysplasia and/or squamous cell carcinoma by visual inspection and palpation. Later histopathological diagnosis indicated that it was not premalignant or malignant but a hyperorthokeratosis and chronic mucositis, which was benign lesion and inflammatory. The histopathological diagnosis is in good agreement with our FLIM results.

6.5 Discussion and conclusion

As described in Chapter 5.7, the total energy deposited over the whole field of view should be smaller than the maximum permissible exposure (MPE) provided by the American National Standards Institute (ANSI) standards for the safe use of lasers on skin [35]. Based on Eq. 5.2, the MPE for this system is $E\ (J) = 5.39 \times 10^{-2} \times (s/f)^{0.25} = 5.39 \times 10^{-2} \times (9847 / 10{,}000)^{0.25} = 53.7$ mJ in a limited aperture of 3.5 mm. The actual energy deposited in an aperture of 3.5 mm is $E\ (J) = 9847 \times 10^{-3}$ mJ = 9.8 mJ, which is lower than the MPE. We are thus confident that *in vivo* imaging with one frame can be performed safely with the proposed handheld FLIM imaging system. The MPE is related to the pixel number per frame and the laser repetition rate. The MPE for different combinations of pixel number per frame and laser repetition rate is summarized in Table 5.

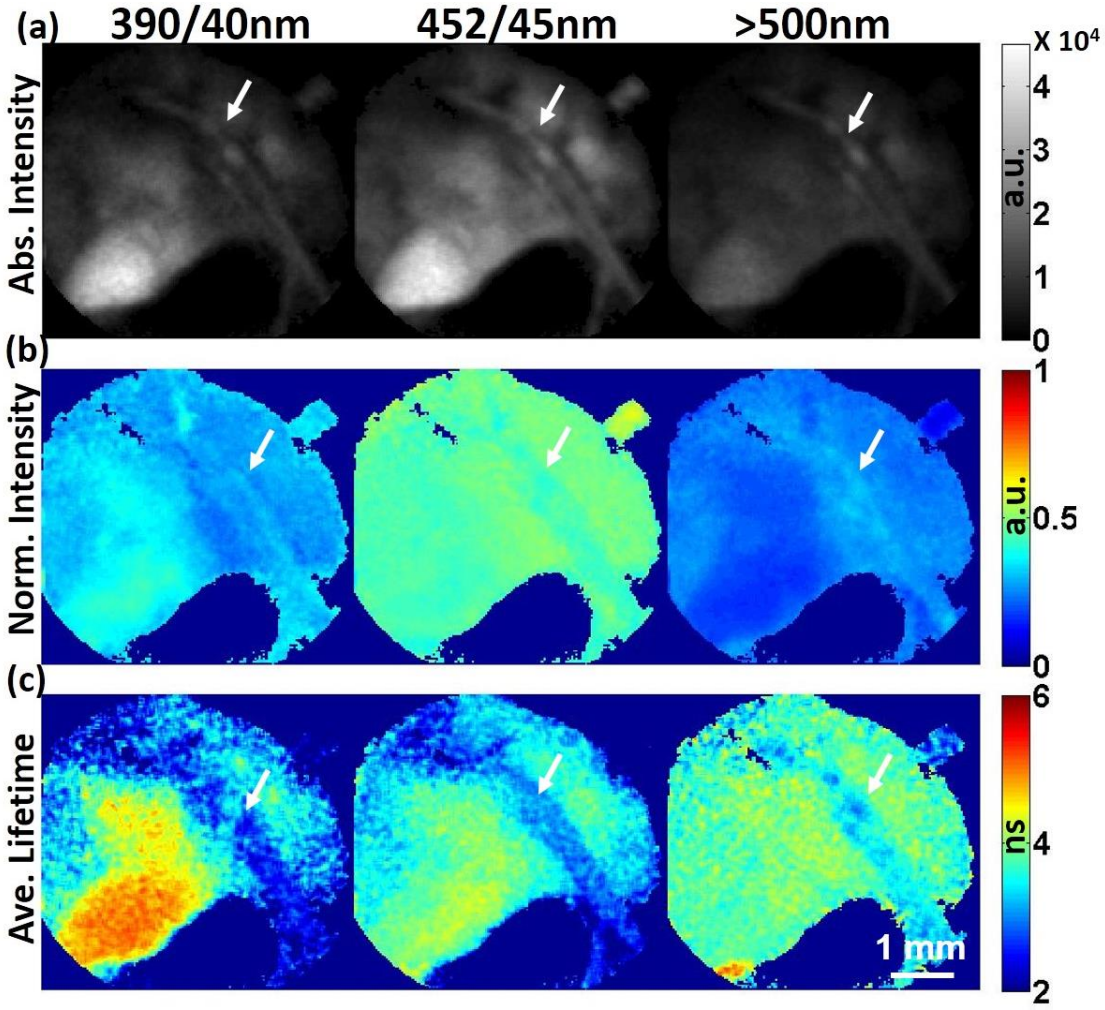

Figure 26: *Ex vivo* imaging of oral biopsy. (a) Absolute integrated fluorescence intensity maps, (b) Normalized integrated fluorescence intensity maps, and (c) Fluorescence lifetime maps. White arrows indicate a piece of hair on the tissue.

In summary, we reported a compact multispectral FLIM endoscope system with rigid probe. This compact version of the handheld FLIM system can help access locations inside the oral cavity which may otherwise be difficult to reach with the larger probe described in previous chapter. We have validated the system with standard fluorescent dye, normal oral mucosa *in vivo* and human biopsy *ex vivo*. This design will be used as clinical

prototype for in vivo study in the future and it will facilitate the evaluation of multispectral FLIM for oral cancer and precancer detection.

Table 5 Comparison table for the MPE and actual deposited energy with different laser repetition rate and pixel number per frame

Pixel number per frame	MPE			Actual Energy
	10K	20K	30K	
80 ×80	38.0 mJ	31.9 mJ	28.8 mJ	2.4 mJ
100 ×100	42.4 mJ	35.7 mJ	32.3 mJ	3.8 mJ
160 ×160	53.7 mJ	45.1 mJ	40.8 mJ	9.8 mJ

7. CONCLUSION AND FUTURE WORK

7.1 Conclusion

In this dissertation, four specific aims were achieved:

First, a bench-top combined FLIM-RCM system was built to determine specific design parameters for endoscope system and characterize the system's performance for detection of oral precancer and cancer. Experiments on hamster cheek pouch model of oral carcinogenesis were conducted. Dysplastic and normal tissue were successfully differentiated.

Second, a flexible endoscope based on a wide-field time-gated implementation was built. The system was validated by a hamster cheek pouch model of oral carcinogenesis. Due to the limitations of this setup, we continued to build a multispectral FLIM system based on pulse sampling implementation for *in vivo* application.

Third, a rigid handheld probe based on pulse sampling was built. Clinical study of human oral tissue was conducted *ex vivo* and *in vivo*.

Fourth, based on the feedback from the physicians who used the handheld FLIM system, a smaller version of the rigid handheld probe was built in order to easily operate and access most of the area inside the oral cavity. The system was validated by imaging normal human oral mucosa *in vivo* and oral biopsy *ex vivo*.

7.2 Future work

More compact design based on novel scanners can be achieved. One possible mechanism is employing a fiber scanner which holds and vibrates the fiber. This design is under investigation by our group. Besides, the dichroic mirror which is used to separate

excitation and emission light can be removed from the handheld box. If a fiber can be used to deliver excitation and emission, the dichroic mirror can be moved to the laser side as shown in Fig. 27. The handheld probe will be modified as a pen-shape device which will be more user-friendly.

More *in vivo* and *ex vivo* imaging of human oral cancer and precancer need to be conducted in order to establish the database for quantitative analysis of the specificity and sensitivity of the FLIM system.

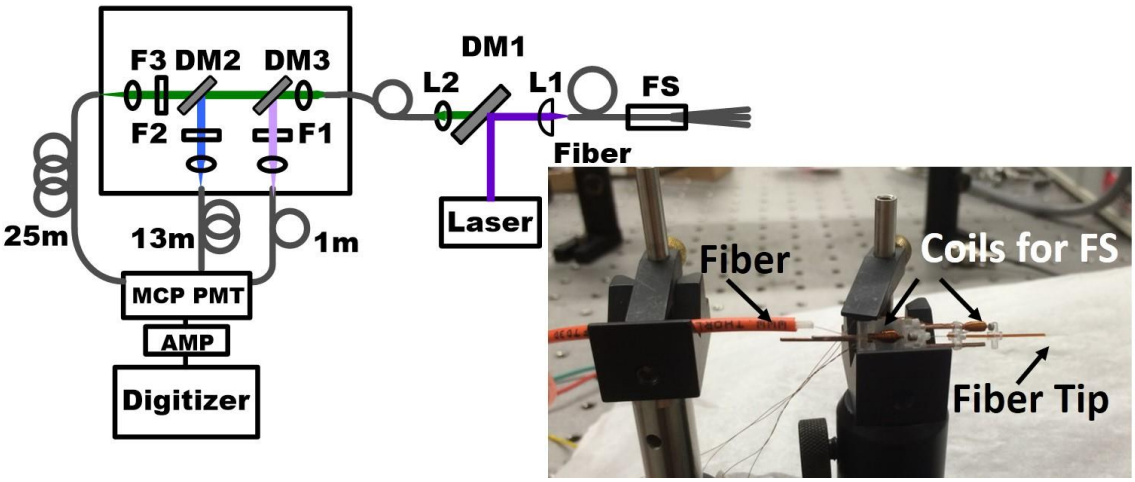

Figure 27: (left) System schematic for the new proposed FLIM endoscope. (right) Photograph to show the appearance of the fiber scanner (FS). DM: Dichroic mirror, L: Lens, F: Filter, AMP: Amplifier.

REFERENCES

1. National Cancer Institute, http://www.cancer.gov/cancertopics/types/oral (2014).
2. R. Siegel, D. Naishadham, and A. Jemal, "Cancer statistics, 2013," CA: A Cancer Journal for Clinicians **63**(1), 11-30 (2013).
3. National Cancer Institute "Seer cancer statistics review, 1975-2011," http://seer.cancer.gov/csr/1975_2011/sections.html (2012).
4. J. R. Lakowicz, *Principles of Fluorescence Spectroscopy*, (Springer, New York, 1983), pp. 1-25.
5. L. Marcu, "Fluorescence lifetime techniques in medical applications," Annals of Biomedical Engineering **40**(2), 304-331 (2012).
6. W. Becker, *The bh TCSPC Handbook*, (Becker & Hickl GmbH, Germany, 2008), pp. 50-350.
7. J. Mizeret et al., "Instrumentation for real-time fluorescence lifetime imaging in endoscopy," Review of Scientific Instruments **70**(12), 4689-4701 (1999).
8. J. Requejo-Isidro et al., "High-speed wide-field time-gated endoscopic fluorescence-lifetimeimaging," Optics Letters **29**(19), 2249-2251 (2004).
9. I. Munro et al., "Toward the clinical application of time-domain fluorescence lifetime imaging," Journal of Biomedical Optics **10**(5), 051403 (2005).
10. G. T. Kennedy, A. J. Thompson, D. S. Elson, M. A. A. Neil, G. W. Stamp, A. Thillainayagam, B. Viellerobe, F. Lacombe, C. Dunsby, and P. M. W. French, "Fluorescence lifetime imaging endoscopy," Proceedings of SPIE, 789308 (2011).

11. H. Sparks et al., "A flexible wide-field FLIM endoscope utilising blue excitation light for label-free contrast of tissue," Journal of Biophotonics 1-11 (2014).

12. G. O. Fruhwirth, R. Cook, T. Watson, T. Ng, and F. Festy, "Fluorescence lifetime endoscopy using TCSPC for the measurement of FRET in live cells," Optics Express **18**(11), 11148-11158 (2010).

13. G. T. Kennedy et al., "A fluorescence lifetime imaging scanning confocal endomicroscope," Journal of Biophotonics **3**, 103-107 (2010).

14. D. S. Elson, J. A. Jo. and L. Marcu, "Miniaturized side-viewing imaging probe for fluorescence lifetime imaging (FLIM): validation with fluorescence dyes, tissue structural proteins and tissue specimens," New Journal of Physics **9**(5), 127 (2007).

15. Y. Sun et al., "Fluorescence lifetime imaging microscopy: *in vivo* application to diagnosis of oral carcinoma," Optics Letters **34**(13), 2081-2083 (2009).

16. P. V. Butte et al., "Fluorescence lifetime spectroscopy for guided therapy of brain tumors," NeuroImage **54**, S125-S135 (2011).

17. J. Bec et al., "Design, construction, and validation of a rotary multifunctional intravascular diagnostic catheter combining multispectral fluorescence lifetime imaging and intravascular ultrasound," Journal of Biomedical Optics **17**(10), 1060121 (2012).

18. Y. Sun et al., "In vivo validation of a bimodal technique combining time-resolved fluorescence spectroscopy and ultrasonic backscatter microscopy for diagnosis of oral carcinoma," Journal of Biomedical Optics **17**(11), 116003 (2012).

19. Z. Nie et al., "Hyperspectral fluorescence lifetime imaging for optical biopsy," Journal of Biomedical Optics **18**(9), 096001 (2013).

20. D. R. Yankelevich et al., "Design and evaluation of a device for fast multispectral time-resolved fluorescence spectroscopy and imaging," Review of Scientific Instruments **85**(3), 034303 (2014).

21. J. M. Jabbour et al., "Fluorescence lifetime imaging and reflectance confocal microscopy for multiscale imaging of oral precancer," Journal of Biomedical Optics **18**(4), 046012 (2013).

22. A. K. Dunn et al., "Sources of contrast in confocal reflectance imaging," Applied Optics **35**(19), 3441-3446 (1996).

23. J. J. Pindborg et al., *Histological Typing of Cancer and Precancer of the Oral Mucosa*, (Springer, Berlin, 1997).

24. P. Pande, and J. A. Jo, "Automated analysis of fluorescence lifetime imaging microscopy (FLIM) data based on the Laguerre deconvolution method," IEEE transactions on bio-medical engineering **58**(1), 172-181 (2011).

25. M. J. Rathbone, *Oral Mucosal Drug Delivery*, (Marcel Dekker Inc., New York 1996).

26. B. L. Luck et al., "An image model and segmentation algorithm for reflectance confocal images of *in vivo* cervical tissue," IEEE Trans Image Process **14**(9), 1265-1276 (2005).

27. S. Cheng et al., "Flexible endoscope for continuous in vivo multispectral fluorescence lifetime imaging," Optics Letters **38**(9), 1515-1517 (2013).

28. J. Siegel et al., "Whole-field five-dimensional fluorescence microscopy combining lifetime and spectral resolution with optical sectioning," Optics Letters **26**(17), 1338-1340 (2001).

29. C. Moore et al., "Comparison of methods for rapid evaluation of lifetimes of exponential decays," Applied Spectroscopy **58**(5), 603-607 (2004).

30. C. W. Chang, and M. A. Mycek, "Enhancing precision in time-domain fluorescence lifetime imaging," Journal of Biomedical Optics **15**(5), 056013 (2010).

31. P. Urayama et al., "A UV–Visible–NIR fluorescence lifetime imaging microscope for laser-based biological sensing with picosecond resolution," Applied Physics B **76**(5), 483-496 (2003).

32. S. Shrestha et al., "High-speed multispectral fluorescence lifetime imaging implementation for in vivo applications," Optics Letters **35**(15), 2558-2560 (2010).

33. S. Cheng et al., "Handheld multispectral fluorescence lifetime imaging system for in vivo applications," Biomedical Optics Express **5**(3), 921-931 (2014).

34. D. G. Ouzounov et al., "Miniature varifocal objective lens for endomicroscopy," Optics Letters **38**(16), 3103-3106 (2013).

35. American National Standard Institute, "Safe Use of Lasers, ANSI Z136.1-2007" (2007).

36. M. Yuvaraj et al., "Fluorescence spectroscopic characterization of salivary metabolites of oral cancer patients," *Journal of Photochemistry and Photobiology B: Biology* **130**, 153-160 (2014).